Degassing of early-formed planetesimals restricted water delivery to Earth

https://doi.org/10.1038/s41586-023-05721-5

Received: 5 May 2022

Accepted: 6 January 2023

Published online: 15 March 2023

Check for updates

M. E. Newcombe[1]✉, S. G. Nielsen[2], L. D. Peterson[1], J. Wang[3], C. M. O'D. Alexander[3], A. R. Sarafian[4], K. Shimizu[5], L. R. Nittler[3,7] & A. J. Irving[6]

The timing of delivery and the types of body that contributed volatiles to the terrestrial planets remain highly debated[1,2]. For example, it is unknown if differentiated bodies, such as that responsible for the Moon-forming giant impact, could have delivered substantial volatiles[3,4] or if smaller, undifferentiated objects were more probable vehicles of water delivery[5–7]. Here we show that the water contents of minerals in achondrite meteorites (mantles or crusts of differentiated planetesimals) from both the inner and outer portions of the early Solar System are ≤2 μg g^{-1} H_2O. These are among the lowest values ever reported for extraterrestrial minerals. Our results demonstrate that differentiated planetesimals efficiently degassed before or during melting. This finding implies that substantial amounts of water could only have been delivered to Earth by means of unmelted material.

Water is one of the most important molecules in the Solar System. It is essential for life, a target of human space exploration and is critical to geologic and planetary processes. Most of the major differentiated bodies in the inner Solar System have been shown to contain water[2], but the origin(s) of that water and the timing of its addition to the terrestrial planets remain uncertain (note that the term 'water' is used in this study to refer to any H-bearing species that could react to form any phase of molecular H_2O, including structurally bound hydroxyl and protons in minerals).

Our meteorite collections preserve a subset of objects that were present in the early Solar System and were possible vehicles of volatile delivery to the proto-Earth. Meteorites (chondrites, achondrites and irons) can generally be divided into 'carbonaceous' (hereafter CC) and 'non-carbonaceous' (hereafter NC) families based on distinct isotopic anomalies (for example, in isotopes of O, Cr, Ti, W and Ni)[8]. This isotopic dichotomy supports the idea that the early Solar System consisted of two distinct chemical reservoirs that were physically separated, either by the growth of Jupiter[9,10] or as a consequence of planetesimal formation at notable condensation fronts in the protoplanetary disk[11,12]. The NCs (including Earth, Mars, the Moon, enstatite chondrites and ordinary chondrites) are thought to have formed in the warmer inner Solar System and the CCs (including carbonaceous chondrites) in the cooler outer Solar System[1,9–12]. Historically, it has been assumed that most NCs accreted little to no water owing to their formation sunward of the snowline—the distance from the Sun beyond which water condenses to ice—whereas the CCs formed beyond the snowline and therefore accreted water ice[13,14]. This assumption, alongside measurements of carbonaceous chondrite-like D/H and volatile element ratios in several terrestrial planets[5,6,15,16], supports the idea that the water on Earth originated from delivery of carbonaceous-chondrite-like material. However, some NC materials such as the ordinary chondrites accreted water ice[13,17,18], and recent work has suggested that the H contents of enstatite chondrites may account for the entire water budget of Earth[19]. In light of the evidence for the presence of water-bearing objects in the NC region during the first few million years of Solar System history and the fact that early-formed terrestrial building blocks probably melted and differentiated, it is important to test the extent to which this water could have been retained during planetesimal differentiation.

Models of planetary accretion processes typically assume that the sizes of the accreting objects had radii of about 1,000–3,500 km (ref. [20]). It is probable that bodies of this size, as well as their earlier-formed planetesimal building blocks, underwent metamorphism, melting and differentiation. Such an inference is supported by thermal models as well as the high abundance of iron meteorites (thought, in most cases, to represent the cores of their parent bodies) found in both CC and NC meteorite families[21,22], suggesting that differentiated parent bodies were common throughout the early Solar System[23–26]. Little is known about how heating and differentiation affects the water budget of a planetesimal, but marked loss of H-bearing species (for example, CH_4, H_2 and H_2O) during metamorphism, melting and degassing from a magma ocean seems inevitable if the planetesimal is not sufficiently large to retain an atmosphere gravitationally[24,27]. At present, it is unclear how efficient these degassing processes were and whether objects retain a memory of their initial water budgets before differentiation. In principle, even if objects that melted lost about 90% of their water, as has been estimated with thermal models[26], differentiated bodies from the CC region that may have originally accreted with >10 wt% water could provide more than enough water to explain the water content of the bulk silicate Earth (approximately 700–3,000 μg g^{-1} H_2O)[7,28]; note that major-element isotopic data have been used to infer a contribution of CC material to the bulk silicate Earth of up to around 40% (ref. [29]), although other studies have argued for much lower CC contributions to the bulk silicate Earth of about 5% (refs. [30,31]). However, we lack constraints on the water budget of meteorites that originated

[1]University of Maryland, College Park, MD, USA. [2]NIRVANA Laboratories, Woods Hole Oceanographic Institution, Woods Hole, MA, USA. [3]Earth and Planets Laboratory, Carnegie Institution for Science, Washington, DC, USA. [4]Corning Incorporated, Corning, NY, USA. [5]University of Wisconsin, Madison, WI, USA. [6]University of Washington, Seattle, WA, USA. [7]Present address: School Of Earth and Space Exploration, Arizona State University, Tempe, AZ, USA. ✉e-mail: newcombe@umd.edu

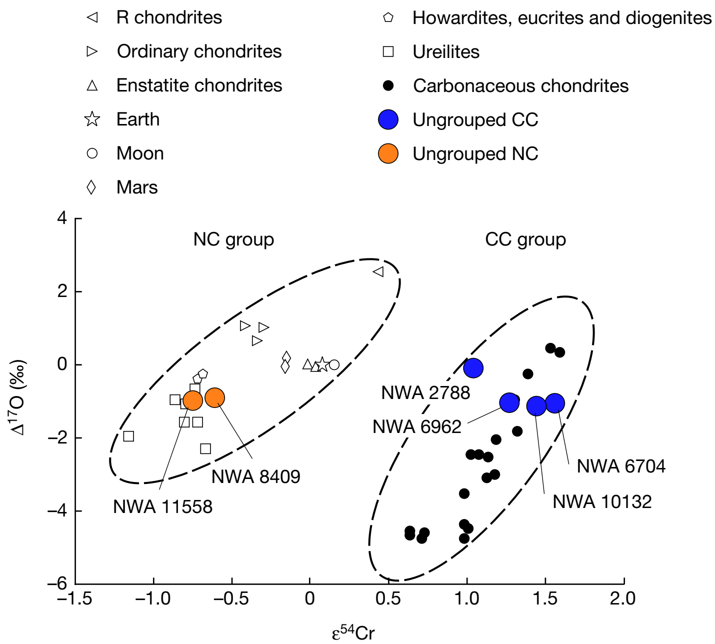

Fig. 1 | Δ^{17}O versus ε^{54}Cr in planetary materials[8]. Ungrouped achondrite meteorites studied here from the NC group are plotted as orange circles and ungrouped achondrite meteorites from the CC group are plotted as blue circles. Note that NWA 8777 is not plotted because no value of ε^{54}Cr has been published for this meteorite. Δ^{17}O of NWA 8777 is −0.291 ± 0.040 ‰ (ref. [49]) and unpublished data suggest that NWA 8777 lies in the NC field (M. Sanborn (personal communication)).

Table 1 | Summary of NC and CC achondrite meteorites analysed

Meteorite	Rock type	Group	Age (Myr)	Parent body	Max. H_2O in NAMs ($\mu g g^{-1}$)
NWA 11558	Tridymite gabbro	NC	4,565	A-NC	<0.6
NWA 8409	Olivine gabbro	NC	4,563	A-NC	<0.6
NWA 8777	Opx-rich metamorphic	NC	nd	B-NC	<2.1
NWA 6962	Brachinite-like	CC	4,564	A-CC	1.0
NWA 2788	Opx-rich metamorphic	CC	nd	B-CC	<0.6
NWA 6704	Px-rich igneous	CC	4,563	C-CC	0.9
NWA 10132	Px-rich igneous	CC	4,563	C-CC	<2.1

nd indicates that no data are available. Orthopyroxene is abbreviated as Opx and low-Ca pyroxene is abbreviated as Px. Parent bodies A-NC, B-NC A-CC, B-CC and C-CC are generic assignments used to indicate meteorites that are paired (that is, from the same parent body). Further description of the mineralogy, group, age and parent-body constraints is provided in Methods.

from differentiated planetesimals that could be used to evaluate this possibility.

Here we investigate the water contents of seven partially or fully differentiated CC and NC ungrouped achondrite meteorites (Fig. 1 and Table 1; see Methods for detailed sample descriptions) from at least five parent bodies that all formed very early (4,563–4,565 Ma; Table 1) in Solar System history. We measured the concentrations of H_2O, F, Cl, S and C in the major igneous minerals found in each meteorite (olivine, orthopyroxene, clinopyroxene and plagioclase) using secondary-ion mass spectrometry (SIMS; Methods). After correction for drift, matrix effects and the analytical blank, we find that—regardless of their origin in the inner or outer Solar System—all minerals in every meteorite that we analysed have extremely low water concentrations (<2 $\mu g\, g^{-1}$, with several samples exhibiting values lower than our blank-corrected detection limit of about 0.6 $\mu g\, g^{-1}$) (Fig. 2 and Extended Data Figs. 1 and 2). We also measured four melt inclusions in the CC achondrite Northwest Africa (NWA) 6962 that contain 10–38 $\mu g\, g^{-1}$ H_2O. Such low water concentrations in melt would be in equilibrium with olivine that contains <0.1 $\mu g\, g^{-1}$ H_2O (ref. [32]), which reinforces the notion of an extremely dry parent body.

Calculating bulk parent-body water contents based on the mineral water contents is associated with large uncertainties (Extended Data Fig. 3 and Methods). However, the melt inclusion water measurements for NWA 6962 remove some of these uncertainties and imply that the bulk parent body for NWA 6962 must have had less water than the 10–38 $\mu g\, g^{-1}$ H_2O we measured in the melt inclusions because water is highly incompatible during both melting and fractional crystallization[33]. The petrogenetic history of NWA 6962 is poorly constrained, but its olivine-rich mineralogy is petrographically similar to the NC brachinite meteorites that are thought to have been generated by crystallization of an approximately 30% partial melt of chondrite-like precursor materials[34]. Assuming that the olivine-hosted melt inclusions we analysed were trapped before substantial crystallization or degassing, their water contents of 10–38 ppm could be generated by 30% melting of a source region containing approximately 3–13 $\mu g\, g^{-1}$ H_2O (Methods and Extended Data Fig. 4). The remaining four parent bodies represented by our measured meteorites would, given that these all exhibit similar or lower water contents in their minerals than in NWA 6962, probably have similar maximum parent-body water contents (Methods).

Altogether, our data imply that, for differentiated, or even only thermally metamorphosed, bodies that are too small to gravitationally retain an atmosphere (about 1,000 km radius for retention of H_2O and CH_4 during thermal metamorphism; see Fig. 3), loss of water and other volatiles is very efficient. Assuming that the CC parent bodies studied here accreted with about 1 wt% water (a low estimate given that the measured and/or estimated initial water contents of all carbonaceous chondrite groups are higher than this[35]), the degassing efficiency of water would have been >99.9%. Alternatively, it is conceivable that the CC achondrite parent bodies accreted dry, from a region of the nebula that was too hot for ice to be present; however, we consider this

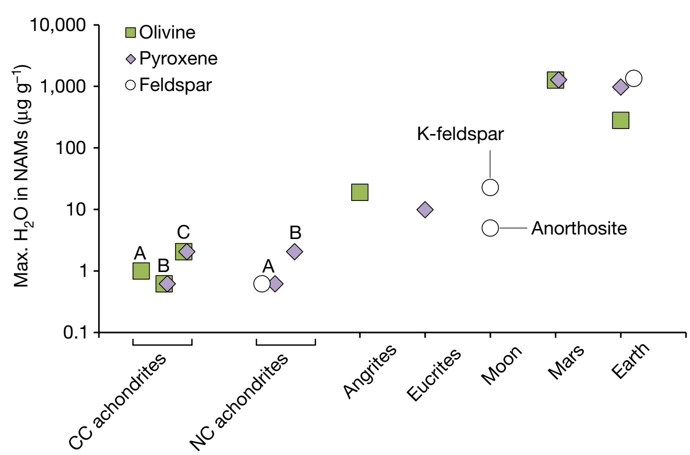

Fig. 2 | Maximum water concentrations measured in NAMs from ungrouped achondrite meteorites (this study), angrites[40], eucrites[41], the Moon[38,39,50], Mars[51,52] and the Earth[53,54]. Three parent bodies (labelled A, B and C) are represented by our ungrouped CC achondrites and two parent bodies (labelled A and B) are represented by our ungrouped NC achondrites (see parent-body designations in Table 1). Two lunar feldspar analyses are shown: analyses of K-feldspar[50] and analyses of plagioclase from ferroan anorthosite and Mg-suite troctolite[39].

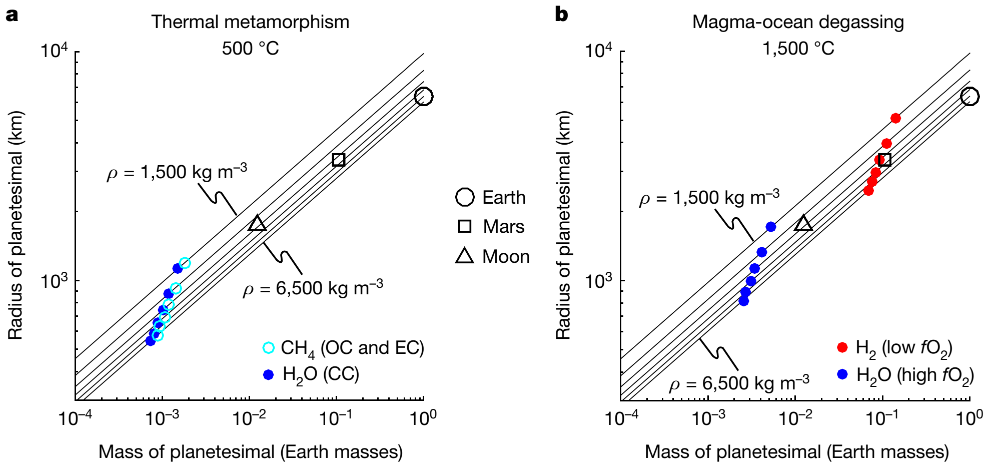

Fig. 3 | Critical radii required for retention of H-bearing species (H_2 in red; H_2O in blue; CH_4 in cyan) at the surface of a growing planetesimal, calculated by equating the thermal velocity of vapour molecules to the escape velocity (which depends on planetesimal density and size). Note that this model does not account for non-thermal atmospheric loss mechanisms (for example, photochemical escape, polar wind escape and impact erosion). See Methods for further details of this approach. **a**, Critical radius for retention of vapour during thermal metamorphism at 500 °C. Modelling and experiments suggest that H_2O is the dominant H-bearing species outgassed during thermal metamorphism of carbonaceous chondrite (CC) precursors and CH_4 is the dominant H-bearing species outgassed from enstatite chondrite (EC) and ordinary chondrite (OC) precursors[27,55,56]. Contours of constant density range from 1,500 kg m^{-3} to 6,500 kg m^{-3} in steps of 1,000 kg m^{-3}. This calculation suggests that planetesimals with radii less than about 1,000 km are unable to retain H_2O or CH_4 vapour during heating by ^{26}Al decay. **b**, Critical radius for retention of vapour during magma-ocean degassing at 1500 °C. Modelling suggests that H_2 is the dominant H-bearing species degassed under low oxygen fugacity (fO$_2$) conditions (more reducing than the iron–wüstite buffer) and H_2O dominates under high fO$_2$ conditions (more oxidizing than the iron–wüstite buffer)[57]. Pressure, temperature and initial volatile budget also affect the speciation and composition of vapour degassed from magma oceans[58] (Methods). Density contours are as in **a**. This calculation shows that planetesimals experiencing local or global magma oceans require a critical radius for retention of H_2 of about 3,400 km and a critical radius for retention of H_2O of about 1,100 km at 1500 °C (assuming a density of around 3,500 kg m^{-3}).

unlikely because CC iron meteorites (thought to represent the cores of differentiated CC parent bodies) are much more oxidized than NC iron meteorites, suggesting that the CC iron meteorites formed in bodies that were initially ice-rich and reaction with this ice oxidized some of the Fe (ref. [36]). The presence of vesicles in NWA 6704 is also suggestive of a hydrous precursor[37]. Our findings suggest that chondritic water may only have been delivered to Earth in substantial amounts by means of bodies that were undifferentiated.

The water concentrations we report here are among the lowest ever measured for extraterrestrial materials (Fig. 2). In particular, the achondrites we analysed contain less water than lunar anorthosites (containing 3–6 μg g^{-1} (refs. [38,39])), in addition to pyroxenes and olivines in angrites[40] and eucrites[41], two NC achondrite groups that originate from the angrite parent body and the asteroid 4 Vesta, respectively. The Moon, angrite parent body and 4 Vesta are strongly depleted in volatile elements (Fig. 2), and what little water they contain is argued to originate from addition of carbonaceous-chondrite-like material after their primary accretion phases were completed[5,15,42]. As such, these bodies may have been as water-depleted as our samples shortly after they differentiated, which underlines the widespread nature of efficient planetary degassing for early-formed parent bodies with <1,000 km radii.

Given the high number of differentiated bodies within the CC group (represented by iron meteorites, pallasites and achondrites from different parent bodies[43]), these must have composed a large fraction of the CC mass that was scattered into the inner Solar System[1]. However, because our data show extremely low water contents in such objects, these would not have been the primary vehicles of water delivery to Earth and the other terrestrial planets. Instead, two categories of bodies may have retained substantial water (wt% levels) until the time when the CC and NC groups began mixing approximately 3–5 Myr after the formation of the Solar System[9,15]. The first consists of small bodies less than about 20 km in diameter, that would not have accumulated sufficient radiogenic heat to have melted[23,26] and, therefore, could have retained a large fraction of their original water. The second consists of objects that accreted later than roughly 1.5 Myr after the start of the Solar System[23,26]. During this period, most radioactive ^{26}Al had decayed, thus preventing differentiation of planetesimals from proceeding for at least the outermost layers[24]. Examples of such objects would be the chondrite parent bodies and Ceres[24,44].

Similar arguments also apply to terrestrial water accretion through other differentiated materials, such as ureilites[4,45] or the Moon-forming impactor[3]. Our results indicate that, for such differentiated bodies to contribute to the water budget of Earth, those bodies must themselves have accreted water-rich, unmelted material, after reaching the critical radius of about 1,000 km required to retain a water-vapour atmosphere (Fig. 3).

Recent work has suggested that the timing of accretionary addition of NC and CC objects can be used to determine the relative timing of volatile addition to Earth[46–48] because CC material was assumed to carry at least an order of magnitude more water than NC material. However, our data show that, for differentiated bodies, such an assumption is incorrect. The presence and quantity of CC-like material is not necessarily related to the timing and quantity of water addition, because some portion of the CC-like material transported to the inner Solar System was probably differentiated and therefore dry.

Our results demonstrate that internal heating and melting of planetesimals results in efficient water loss, producing a planetary feedstock that is similarly depleted in water regardless of whether that material accreted in the inner or (ice-rich) outer Solar System. Thermal models demonstrate that planetesimal size and accretion age are the most important parameters that control the internal temperature, and therefore the water content, of planetesimals. Further modelling work that focuses on the relative mass flux of objects with varying sizes and accretion ages over the later stages of Earth's accretion history will be needed in the future to put constraints on the probable water contents of NC (including enstatite and ordinary chondrites) and CC (including carbonaceous chondrites) objects that were added to Earth.

Online content

Any methods, additional references, Nature Portfolio reporting summaries, source data, extended data, supplementary information, acknowledgements, peer review information; details of author contributions and competing interests; and statements of data and code availability are available at https://doi.org/10.1038/s41586-023-05721-5.

1. O'Brien, D. P., Izidoro, A., Jacobson, S. A., Raymond, S. N. & Rubie, D. C. The delivery of water during terrestrial planet formation. *Space Sci. Rev.* **214**, 47 (2018).
2. McCubbin, F. M. & Barnes, J. J. Origin and abundances of H_2O in the terrestrial planets, Moon, and asteroids. *Earth Planet. Sci. Lett.* **526**, 115771 (2019).
3. Grewal, D. S., Dasgupta, R., Sun, C., Tsuno, K. & Costin, G. Delivery of carbon, nitrogen, and sulfur to the silicate Earth by a giant impact. *Sci. Adv.* **5**, eaau3669 (2019).
4. Hirschmann, M. M. Constraints on the early delivery and fractionation of Earth's major volatiles from C/H, C/N, and C/S ratios. *Am. Mineral.* **101**, 540–553 (2016).
5. Sarafian, A. R., Nielsen, S. G., Marschall, H. R., McCubbin, F. M. & Monteleone, B. D. Early accretion of water in the inner solar system from a carbonaceous chondrite-like source. *Science* **346**, 623–626 (2014).
6. Alexander, C. M. O'D. et al. The provenances of asteroids, and their contributions to the volatile inventories of the terrestrial planets. *Science* **337**, 721–723 (2012).
7. Marty, B. The origins and concentrations of water, carbon, nitrogen and noble gases on Earth. *Earth Planet. Sci. Lett.* **313**, 56–66 (2012).
8. Warren, P. H. Stable-isotopic anomalies and the accretionary assemblage of the Earth and Mars: a subordinate role for carbonaceous chondrites. *Earth Planet. Sci. Lett.* **311**, 93–100 (2011).
9. Kruijer, T. S., Burkhardt, C., Budde, G. & Kleine, T. Age of Jupiter inferred from the distinct genetics and formation times of meteorites. *Proc. Natl Acad. Sci.* **114**, 6712–6716 (2017).
10. Walsh, K. J., Morbidelli, A., Raymond, S. N., O'Brien, D. P. & Mandell, A. M. A low mass for Mars from Jupiter's early gas-driven migration. *Nature* **475**, 206–209 (2011).
11. Morbidelli, A. et al. Contemporary formation of early Solar System planetesimals at two distinct radial locations. *Nat. Astron.* **6**, 72–79 (2022).
12. Izidoro, A. et al. Planetesimal rings as the cause of the Solar System's planetary architecture. *Nat. Astron.* **6**, 357–366 (2022).
13. Alexander, C. M. O'D., McKeegan, K. D. & Altwegg, K. Water reservoirs in small planetary bodies: meteorites, asteroids, and comets. *Space Sci. Rev.* **214**, 36 (2018).
14. Morbidelli, A. et al. Fossilized condensation lines in the Solar System protoplanetary disk. *Icarus* **267**, 368–376 (2016).
15. Sarafian, A. R. et al. Early accretion of water and volatile elements to the inner Solar System: evidence from angrites. *Philos. Trans. R. Soc. A Math. Phys. Eng. Sci.* **375**, 20160209 (2017).
16. Saal, A. E., Hauri, E. H., Van Orman, J. A. & Rutherford, M. J. Hydrogen isotopes in lunar volcanic glasses and melt inclusions reveal a carbonaceous chondrite heritage. *Science* **340**, 1317–1320 (2013).
17. Alexander, C. M. O'D., Barber, D. J. & Hutchison, R. The microstructure of Semarkona and Bishunpur. *Geochim. Cosmochim. Acta* **53**, 3045–3057 (1989).
18. Robert, F., Merlivat, L. & Javoy, M. Deuterium concentration in the early Solar System: hydrogen and oxygen isotope study. *Nature* **282**, 785–789 (1979).
19. Piani, L. et al. Earth's water may have been inherited from material similar to enstatite chondrite meteorites. *Science* **369**, 1110–1113 (2020).
20. O'Brien, D. P., Walsh, K. J., Morbidelli, A., Raymond, S. N. & Mandell, A. M. Water delivery and giant impacts in the 'Grand Tack' scenario. *Icarus* **239**, 74–84 (2014).
21. Sanborn, M. E. & Yin, Q.-Z. in *Proc. 50th Lunar and Planetary Science Conference 2019*, LPI contribution no. 2132, id. 1498 (2019).
22. Budde, G. et al. Molybdenum isotopic evidence for the origin of chondrules and a distinct genetic heritage of carbonaceous and non-carbonaceous meteorites. *Earth Planet. Sci. Lett.* **454**, 293–303 (2016).
23. Hevey, P. J. & Sanders, I. S. A model for planetesimal meltdown by ^{26}Al and its implications for meteorite parent bodies. *Meteorit. Planet. Sci.* **41**, 95–106 (2006).
24. Elkins-Tanton, L. T. Magma oceans in the inner solar system. *Annu. Rev. Earth Planet. Sci.* **40**, 113–139 (2012).
25. McSween, H. Y. Jr, Ghosh, A., Grimm, R. E., Wilson, L. & Young, E. D. in *Asteroids III* (eds Bottke, W. F., Cellino, A., Paolicchi, P. & Binzel, R. P.) 559–571 (Univ. Arizona Press, 2002).
26. Lichtenberg, T. et al. A water budget dichotomy of rocky protoplanets from ^{26}Al-heating. *Nat. Astron.* **3**, 307–313 (2019).
27. Schaefer, L. & Fegley, B. Outgassing of ordinary chondritic material and some of its implications for the chemistry of asteroids, planets, and satellites. *Icarus* **186**, 462–483 (2007).
28. Hirschmann, M. M. Comparative deep Earth volatile cycles: the case for C recycling from exosphere/mantle fractionation of major (H_2O, C, N) volatiles and from H_2O/Ce, CO_2/Ba, and CO_2/Nb exosphere ratios. *Earth Planet. Sci. Lett.* **502**, 262–273 (2018).
29. Schiller, M., Bizzarro, M. & Fernandes, V. A. Isotopic evolution of the protoplanetary disk and the building blocks of Earth and the Moon. *Nature* **555**, 507–510 (2018).
30. Dauphas, N. The isotopic nature of the Earth's accreting material through time. *Nature* **541**, 521–524 (2017).
31. Hopp, T., Dauphas, N., Spitzer, F., Burkhardt, C. & Kleine, T. Earth's accretion inferred from iron isotopic anomalies of supernova nuclear statistical equilibrium origin. *Earth Planet. Sci. Lett.* **577**, 117245 (2022).
32. Newcombe, M. E., Plan, T., Asimow, P. D., Barth, A. & Hauri, E. Water-in-olivine magma ascent chronometry: every crystal is a clock. *J. Volcanol. Geotherm. Res.* **398**, 106872 (2020).
33. Hauri, E. H., Gaetani, G. A. & Green, T. H. Partitioning of water during melting of the Earth's upper mantle at H_2O-undersaturated conditions. *Earth Planet. Sci. Lett.* **248**, 715–734 (2006).
34. Mittlefehldt, D. W., Bogard, D. D., Berkley, J. L. & Garrison, D. H. Brachinites: igneous rocks from a differentiated asteroid. *Meteorit. Planet. Sci.* **38**, 1601–1625 (2003).
35. Alexander, C. M. O'D. Quantitative models for the elemental and isotopic fractionations in chondrites: the carbonaceous chondrites. *Geochim. Cosmochim. Acta* **254**, 277–309 (2019).
36. Spitzer, F., Burkhardt, C., Nimmo, F. & Kleine, T. Nucleosynthetic Pt isotope anomalies and the Hf-W chronology of core formation in inner and outer solar system planetesimals. *Earth Planet. Sci. Lett.* **576**, 117211 (2021).
37. Sanborn, M. E. et al. Carbonaceous achondrites Northwest Africa 6704/6693: milestones for early Solar System chronology and genealogy. *Geochim. Cosmochim. Acta* **245**, 577–596 (2019).
38. Hui, H., Peslier, A. H., Zhang, Y. & Neal, C. R. Water in lunar anorthosites and evidence for a wet early Moon. *Nat. Geosci.* **6**, 177–180 (2013).
39. Hui, H. et al. A heterogeneous lunar interior for hydrogen isotopes as revealed by the lunar highlands samples. *Earth Planet. Sci. Lett.* **473**, 14–23 (2017).
40. Sarafian, A. R. et al. Angrite meteorites record the onset and flux of water to the inner solar system. *Geochim. Cosmochim. Acta* **212**, 156–166 (2017).
41. Sarafian, A. R. et al. The water and fluorine content of 4 Vesta. *Geochim. Cosmochim. Acta* **266**, 568–581 (2019).
42. Hauri, E. H., Saal, A. E., Rutherford, M. J. & Van Orman, J. A. Water in the Moon's interior: truth and consequences. *Earth Planet. Sci. Lett.* **409**, 252–264 (2015).
43. Rubin, A. E. Carbonaceous and noncarbonaceous iron meteorites: differences in chemical, physical, and collective properties. *Meteorit. Planet. Sci.* **53**, 2357–2371 (2018).
44. Fu, R. R. et al. The interior structure of Ceres as revealed by surface topography. *Earth Planet. Sci. Lett.* **476**, 153–164 (2017).
45. Barrat, J.-A., Sansjofre, P., Yamaguchi, A., Greenwood, R. C. & Gillet, P. Carbon isotopic variation in ureilites: evidence for an early, volatile-rich Inner Solar System. *Earth Planet. Sci. Lett.* **478**, 143–149 (2017).
46. Budde, G., Burkhardt, C. & Kleine, T. Molybdenum isotopic evidence for the late accretion of outer Solar System material to Earth. *Nat. Astron.* **3**, 736–741 (2019).
47. Fischer-Gödde, M. et al. Ruthenium isotope vestige of Earth's pre-late-veneer mantle preserved in Archaean rocks. *Nature* **579**, 240–244 (2020).
48. Kruijer, T. S., Kleine, T. & Borg, L. E. The great isotopic dichotomy of the early Solar System. *Nat. Astron.* **4**, 32–40 (2020).
49. Irving, A. J., Kuehner, S. M. & Ziegler, K. in *Proc. 78th Annual Meeting of the Meteoritical Society*, LPI contribution no. 1856, p. 5254 (2015).
50. Mills, R. D., Simon, J. I., Alexander, C. M. O'D., Wang, J. & Hauri, E. H. Water in alkali feldspar: the effect of rhyolite generation on the lunar hydrogen budget. *Geochem. Perspect. Lett.* **3**, 115–123 (2017).
51. Hallis, L. et al. Effects of shock and Martian alteration on Tissint hydrogen isotope ratios and water content. *Geochim. Cosmochim. Acta* **200**, 280–294 (2017).
52. Mane, P. et al. Hydrogen isotopic composition of the Martian mantle inferred from the newest Martian meteorite fall, Tissint. *Meteorit. Planet. Sci.* **51**, 2073–2091 (2016).
53. Peslier, A. H. A review of water contents of nominally anhydrous natural minerals in the mantles of Earth, Mars and the Moon. *J. Volcanol. Geotherm. Res.* **197**, 239–258 (2010).
54. Johnson, E. A. & Rossman, G. R. A survey of hydrous species and concentrations in igneous feldspars. *Am. Mineral.* **89**, 586–600 (2004).
55. Schaefer, L. & Fegley, B. Jr Chemistry of atmospheres formed during accretion of the Earth and other terrestrial planets. *Icarus* **208**, 438–448 (2010).
56. Thompson, M. A. et al. Composition of terrestrial exoplanet atmospheres from meteorite outgassing experiments. *Nat. Astron.* **5**, 575–585 (2021).
57. Gaillard, F. et al. Redox controls during magma ocean degassing. *Earth Planet. Sci. Lett.* **577**, 117255 (2022).
58. Gaillard, F. & Scaillet, B. A theoretical framework for volcanic degassing chemistry in a comparative planetology perspective and implications for planetary atmospheres. *Earth Planet. Sci. Lett.* **403**, 307–316 (2014).

Methods

Sample descriptions

Tridymite gabbro NC meteorite NWA 11558. NC meteorite NWA 11558 has a distinct green and white porphyritic texture dominated by large (approximately 1.6–2.1 mm) anorthite grains, compositionally zoned clinopyroxene and tridymite (characterized by A. Irving and S. Kuehner of UWS, and I. Barker and D. Moser of UWO[59]). Groundmass phases include bytownite plagioclase, clinopyroxene, orthopyroxene, ilmenite, ulvospinel, troilite, cristobalite, quartz, low-Ni kamacite and baddeleyite[59]. NWA 11558 is paired with NWA 11119 based on the identical oxygen-isotope compositions reported for these meteorites[59] and their similar mineralogy. This meteorite seems to originate from the same parent body as paired meteorites NWA 7325 and NWA 8409 (measured by K. Ziegler of UNM[1]). NWA 11119 (paired with NWA 11558) has an Al–Mg crystallization age of about 4,565 Myr (ref. [60]), suggesting that this group of meteorites formed in the presence of the solar nebula.

Olivine gabbro NC meteorite NWA 8409. NWA 8409 has a gabbroic composition dominated by pyroxene, olivine and plagioclase[60,61]. This meteorite has been paired with NWA 7325 and is in the NC field[62]. The age of NWA 8409 is estimated to be around 4,563 Myr (ref. [60]).

Brachinite-like CC meteorite NWA 6962. NWA 6962 is petrographically similar (but isotopically distinct) to brachinites, being dominated by large (approximately 750 μm), equant olivine grains (with composition $Fa_{47.1-47.9}$) set in an interstitial matrix of intergrown plagioclase and clinopyroxene[62]. Sparse grains of Ti-poor chromite, kamacite, iron sulfide and merrillite are also present. Silicate melt inclusions containing quenched melt with a sodic plagioclase composition, chromite and Ni-free metal are common in the olivine grains[63,64]. In the main text, we report the volatile content of four of these melt inclusions. It has been proposed that the NWA 6962 olivines are cumulates, and melting experiments suggest that NWA 6962 olivine compositions can be produced by crystallization of a CR-chondrite melt[63].

Low-Ca pyroxene-rich NC and CC meteorites. The mineralogy of NWA 8777, NWA 2788, NWA 6704 and NWA 10132 are all dominated by low-Ca pyroxene[65]. All samples except NWA 6704 have evidence of thermal overprinting[66,67], whereas primary igneous zonation is evident in NWA 6704, which probably formed during supercooling of a melt[62,67]. This meteorite also has reported melt inclusions as well as vesicles that seem to bear evidence of volatile exsolution[66]. NWA 8777 and NWA 2788 exhibit metamorphic textures that were probably produced by thermal metamorphism or partial melting of chondritic precursors[66]. On the basis of their Cr and O isotope compositions (see Fig. 1 and Table 1), these four meteorites probably represent three different parent bodies from both the NC and CC fields: NWA 8777 is in the NC field (M. Sanborn (personal communication)), NWA 2788 is in the CC field[68] and NWA 6704 and NWA 10132 are thought to be from the same parent body in the CC field[67] (notably, NWA 6704 is paired with NWA 6693 and NWA 6926 (ref. [69]), so this parent body is well represented in the meteorite record relative to the parent bodies of other ungrouped achondrites). The ages of the meteorites are about 4,563 Myr for NWA 6704 (refs. [37,66]) and NWA 10132 (ref. [70]). Chronological data have not yet been reported for NWA 2788 and NWA 8777.

Sample preparation and analytical techniques

Sample preparation. Meteorite chips and secondary standards (Suprasil glass, Herasil glass, ALV-519-4-1) were mounted in dental resin and polished to 0.25 μm using alumina papers and diamond paste. The dental resin was dissolved in acetone overnight and contamination from residual dental resin was removed by ultrasonicating the meteorite chips and standards in three cycles each of toluene, acetone and isopropanol. The samples and standards were then placed in a vacuum oven at approximately 100 °C for >24 h before being pressed into indium. A final polish of the indium mounts in 0.3-μm alumina paste on Buehler MicroCloth was used to remove indium from the surfaces of the grains, to improve the contact between the indium and the grain edges and to enhance the topography at grain edges within the crystalline meteorite chips to aid identification of individual grains during analysis by SIMS. The indium mounts were then coated in iridium and mapped by scanning electron microscopy (SEM). Following the SEM analyses, the iridium coating was removed and the mounts were placed in a vacuum oven at about 60 °C overnight before being coated in gold (to prevent charge build-up during SIMS analysis). After gold coating, the samples were placed in the airlock chamber of the IMS-6f SIMS instrument at Carnegie Earth and Planets Laboratory for one week to three months before analysis to reduce the analytical blank. Finally, the gold coat was removed and the samples were carbon-coated and analysed by electron microprobe analysis (EPMA).

Mapping of sample topography and composition by SEM. The 1-inch-round mounts containing our polished meteorite chips were imaged with the Zeiss Auriga SEM at the Carnegie Earth and Planets Laboratory. Secondary and backscattered electron (BSE) images were collected for each meteorite chip and energy-dispersive X-ray spectroscopy (EDS) was used to create maps of elemental concentrations that were used to identify and distinguish different mineral phases. Barnes et al.[71] warn that the use of high beam currents on minerals such as apatite may cause mobility of H that could potentially affect subsequent analyses of water concentration and D/H. In light of this work, we used a 30-μm aperture such that the effective beam current applied to the surface of our sample was about 0.7 nA. Photomicrographs, EDS and BSE maps of our meteorite chips are provided in Extended Data Figs. 5–12.

Analysis of highly volatile elements and P by SIMS. Concentrations of H_2O, CO_2, S, Cl, F and P were characterized using the Cameca IMS-6f ion microprobe at the Carnegie Earth and Planets Laboratory, following established analytical protocols[32,72–75]. The vacuum in the analysis chamber was maintained at a pressure of approximately $3-6 \times 10^{-10}$ torr. The Cs^+ primary beam was tuned to achieve a current of about 15–23 nA with an approximate beam diameter of 20 μm. Charge compensation was provided by an electron flood gun. Before data collection, the sample area was pre-sputtered for 3 min with the rastered primary beam to remove the gold coat and surface contamination. During data collection, a field aperture was used to ensure the collection of ions from only the central approximately 5 μm of the measurement area. Negatively charged $^{12}C^-$, $^{16}O^1H^-$, $^{19}F^-$, $^{30}Si^-$, $^{31}P^-$, $^{32}S^-$ and $^{35}Cl^-$ ions were detected using an electron multiplier detector, with five cycles of data collected at each point. Occasionally, one or more cycles recorded zero counts owing to an electrical glitch; these cycles were deleted. The mass-resolving power was sufficient to resolve $^{16}O^1H^-$ from $^{17}O^-$.

Analysis of major elements by electron microprobe. Following SIMS analysis, major, minor and trace element concentrations in individual mineral grains were measured using the JXA 8900R electron microprobe at the University of Maryland. Analyses were conducted with a beam current of 25 nA, an accelerating potential of 15 keV and a focused beam with a nominal diameter of 1 μm. We used on-peak counting times of 20 s for iron and 30 s for all other elements. We applied atomic number, absorption and fluorescence corrections to our raw X-ray intensities. Olivine analyses were standardized as follows: San Carlos olivine: Fe, Mg, Si, Ni; Kakanui augite: Ca, Al; hypersthene: Cr; fayalite: Mn; Kakanui hornblende: Ti. Pyroxene and feldspar analyses were standardized as follows: Kakanui hornblende: Fe, Ti; Kakanui augite: Ca, Mg, Al, Si; fayalite: Mn; San Carlos olivine: Ni; hypersthene: Cr. Electron-microprobe data are provided in the Supplementary Data Tables.

Data processing

Reduction and calibration of SIMS data. Data reduction and calibration were approached following a previously developed protocol[75]. Counts of volatile and $^{31}P^-$ ions were first divided by counts of $^{30}Si^-$ to account for instrumental drift (for example, caused by fluctuations in primary beam current) and multiplied by SiO_2/50 (in which SiO_2 is the silica concentration of the sample in wt% as measured by electron microprobe; Supplementary Data Tables). Analyses of $^{16}O^1H/^{30}Si^-$ are particularly sensitive to instrumental drift, so this was further corrected for our March 2019 data by applying a drift correction based on a piecewise linear function fit to frequent analyses of $^{16}O^1H/^{30}Si^-$ in Herasil glass (Supplementary Data Tables). Our May 2019 data exhibit minimal drift (replicate analyses of ALV-519-4-1 vary within 2% relative standard deviations), so a time-dependent drift correction was not applied to the May data. To correct for shifts in the H_2O calibration from the standard mount to the sample mounts, $^{16}O^1H/^{30}Si^-$ analyses on each mount were multiplied by a 'K-factor' equal to the average $^{16}O^1H/^{30}Si^-$ of glass standard ALV-519-4-1 measured on the standard mount divided by the average $^{16}O^1H/^{30}Si^-$ of ALV-519-4-1 measured on the sample mount[75].

Assessments of the analytical blank and the detection limit (as previously defined[76]) were made using replicate analyses of synthetic forsterite 'GRR 3649' (provided by G. Rossman) and 'Suprasil 3002' glass (Extended Data Fig. 1). During both of our analytical sessions (February–March 2019 and May 2019), the detection limits were <0.91 μg g^{-1} CO_2, less than about 2 μg g^{-1} H_2O, <0.11 μg g^{-1} F, <0.03 μg g^{-1} P, <0.22 μg g^{-1} S and <0.06 μg g^{-1} Cl (note that synthetic forsterite was not measured during the March session and Suprasil is not a suitable blank for Cl, so the detection limit for Cl during the March session is poorly constrained). Analyses presented in Extended Data Fig. 1 are not blank-corrected.

We blank-corrected the H_2O data from our May 2019 session by subtracting time-dependent $^{16}O^1H/^{30}Si*SiO_2/50$ measured in nominally dry synthetic forsterite GRR 3649 from $^{16}O^1H/^{30}Si*SiO_2/50$ measured in our unknowns (we approximate the time dependence of the blank using a piecewise linear function of $^{16}O^1H/^{30}Si*SiO_2/50$; Supplementary Data Tables). Our blank-corrected data have a detection limit of about 0.62 μg g^{-1} H_2O (calculated as three times the standard deviation of H_2O measurements of synthetic forsterite GRR 3649; Extended Data Fig. 2). During our March 2019 session, we used Suprasil 3002 glass to monitor the blank. We have compiled analyses of synthetic forsterite and Suprasil 3002 glass over three analytical sessions that allow us to quantify a blank-corrected H_2O concentration in Suprasil 3002 glass of 2.00 ± 0.43 μg g^{-1} H_2O (the uncertainty is reported as one standard deviation of 21 analyses). We note that previous studies[15,32,40] have assumed a value of <1 μg g^{-1} H_2O in Suprasil 3002, based on infrared laser-absorption measurements in documentation provided by glass manufacturer Heraeus (https://www.heraeus.com/media/media/hca/doc_hca/products_and_solutions_8/optics/Fused_Silica_for_Applications_in_the_NIR_EN.pdf; retrieved July 2021). This documentation states that "During the manufacturing process an intermediate drying step reduces the OH content of the Suprasil 300 grades to below 1 ppm." H_2O concentrations in Suprasil 3002 as measured by infrared laser absorption are lower than our SIMS-based estimate of 2 μg g^{-1} H_2O. We propose that this discrepancy may be the result of H_2 dissolution in Suprasil 3002 glass that is readily measured by SIMS but is only weakly infrared-active[77]. Assuming a concentration of 2 μg g^{-1} H_2O in Suprasil 3002 glass, we estimate that our analytical blank during our March 2019 session is roughly 1.6 μg g^{-1} H_2O, with a corresponding blank-corrected detection limit of about 2 μg g^{-1} H_2O. Blank-corrected H_2O concentrations are shown in Extended Data Fig. 2.

Blank-corrected S, F and Cl concentrations are shown in Extended Data Fig. 2. Our analytical blank for S and F analyses was estimated using replicate analyses of Suprasil 3002 glass. The blank correction was performed by subtracting average values of $X/^{30}Si*SiO_2/50$ in Suprasil 3002 from $X/^{30}Si*SiO_2/50$ in the unknowns (in which 'X' represents ^{32}S and ^{19}F). Similarly, Cl analyses were blank-corrected by subtracting the average $^{35}Cl/^{30}Si*SiO_2/50$ measured in synthetic forsterite GRR 3649 from $^{35}Cl/^{30}Si*SiO_2/50$ measured in our unknowns (this correction was only possible during our May 2019 session).

Selections of basaltic glasses and grains of olivine, orthopyroxene and clinopyroxene with well-characterized volatile contents were used as standards (Supplementary Data Tables). Calibrations of absolute water concentrations in olivine are as present subject to uncertainties of about 30 rel% owing to uncertainties in the absorption coefficients used to measure the water concentrations of the standards by Fourier-transform infrared spectroscopy[78,79]. Further uncertainty in the olivine calibration arises from well-documented heterogeneities in the olivine standards[74]. Several studies have demonstrated that the calibration curves for orthopyroxene and olivine are similar, with regression-line slopes that vary within roughly 20% (refs. [73,80]); therefore, given the aforementioned uncertainty in the olivine calibration, we decided in this study to calibrate our olivine measurements using orthopyroxene standards[75,81]. Our dataset includes a few analyses of feldspar and quartz, for which matrix-matched calibration standards were unavailable, so we applied our glass calibrations to these analyses. We provide analyses of our standards (including the olivine standards) in the Supplementary Data Tables.

After calibrating our analyses as described above, we screened our dataset for outliers. Nominally anhydrous mineral (NAM) analyses with $^{12}C/^{30}Si > 3 \times 10^{-10}$ were excluded on the basis of the likelihood that these data were affected by surface contamination. These outliers (<3% of the total number of analyses) are labelled in the Supplementary Data Tables.

Further description of results

Measurements of highly volatile elements in CC and NC ungrouped meteorites are plotted in Extended Data Fig. 1. Most of our highly volatile element analyses in NAMs fall at or below the detection limit, with the exception of F (which is detectable in NWA 8777, NWA 2788, NWA 11558 and NWA 8409) and S (which is detectable in NWA 8409 and NWA 11558). Analyses of Cl during our March 2019 analytical session suffered an issue with the detector, such that we were unable to consistently reproduce the known Cl concentration in secondary standard ALV-519-4-1, so we exclude Cl analyses from this session in the discussion below (this affects Cl analyses of NWA 8777 and NWA 10132). As well as our analyses of NAMs, we analysed four olivine-hosted melt inclusions in NWA 6962.

All of the meteorites we analysed are extraordinarily dry: none of the measured water concentrations in NAMs exceed the water concentration of Suprasil 3002 glass (about 2 μg g^{-1}), which is used by several research groups as an analytical blank. Some of our meteorite NAM analyses fall consistently below our estimate of the analytical blank (based on replicate analyses of synthetic forsterite and/or Suprasil 3002 glass) (Fig. 2). This could indicate that our blank materials contain higher volatile contents than some of the meteorite NAMs. If so, we may have overestimated our blank, resulting in underestimated blank-corrected concentrations (Extended Dada Fig. 2). Alternatively, the apparent offsets between meteorite and blank analyses could be a result of matrix effects because neither of our blank materials is perfectly matrix-matched to the meteorite NAMs: Suprasil glass, containing 100% SiO_2, is a particularly poor matrix match to our unknowns; and synthetic forsterite is also an imperfect match to the meteorite NAMs, several of which contain high concentrations of FeO (Supplementary Data Tables). SIMS analyses of amphibole and mica demonstrate that H/Si increases with increasing Fe concentration[73], which may be explained as a matrix effect related to the associated increase in the mean molecular weight of the matrix[82]; however, Mosenfelder and Rossman[80] show that SIMS analyses of orthopyroxene ranging in Mg number from 79 to 99 do not show statistically resolvable Fe-related matrix effects. Given the large range of Mg number documented in meteorite NAMs, the importance of Fe-related matrix effects on H/Si yield during SIMS analyses of NAMs warrants further study.

In Extended Data Fig. 2, we present blank-corrected analyses of volatiles in NAMs. Analyses that fall below the detection limit are plotted along the *x* axis (that is, at 0 μg g^{-1} for H_2O, S and Cl, and at 0.01 μg g^{-1} for F). Olivine grains in NWA 6704 and NWA 6962 are the only grains that contain detectable H_2O; however, these grains also contain elevated concentrations of CO_2, suggesting surface contamination of these analyses (Extended Data Fig. 1a), and coexisting orthopyroxene in NWA 6704 does not contain detectable water. Furthermore, we measured four olivine-hosted melt inclusions containing 10–38 μg g^{-1} H_2O in NWA 6962 that would be in equilibrium with olivine containing approximately 0.01–0.05 μg g^{-1} H_2O (applying an olivine–melt partition coefficient of 0.0014 (ref. [33])); that is, a much lower concentration than our measured value. These lines of reasoning suggest that the detectable H_2O in NWA 6704 and NWA 6962 olivines could be a result of minor surface contamination.

Crustal lithologies NWA 8409 (gabbroic) and NWA 11558 (andesitic) contain detectable F and S, consistent with the enrichment of these incompatible elements in the melt phase during partial melting of their parent body. Excluding the F and S concentrations measured in these crustal lithologies, the most important observations from our data are that all of our meteorites are nominally dry (the NAMs contain <2 μg g^{-1} H_2O) and there is no systematic difference between the volatile contents of the CC-affinity and NC-affinity samples.

Application of mineral–melt and mineral–mineral partition coefficients to estimate bulk volatile contents of parent bodies. Evidence in the literature suggests that most of the meteorites we analysed represent the products of crystallization from silicate melt; for example, NWA 11558 has a porphyritic texture typical of a volcanic igneous rock and the other six meteorites have textures typical of igneous cumulates (that is, large, equant grains in a fine-grained interstitial matrix). Under the assumption that the NAM grains we analysed are the products of crystallization from silicate melt, we can apply mineral–melt partition coefficients to our measured volatile concentrations to calculate the volatile content of the melts from which the NAMs crystallized. It is unclear whether NWA 8777 and NWA 2788 experienced partial melting or whether these meteorites are the products of thermal metamorphism of chondritic precursor materials[68]; however, we include these meteorites in the following analysis for ease of comparison with our other samples.

Most of our NAM H_2O analyses are at or close to the detection limit, which we estimate to be about 2 μg g^{-1} (blank-corrected) during our March 2019 session and about 0.62 μg g^{-1} H_2O (blank-corrected) during our May 2019 session. These analyses allow us to place an upper bound on the amount of H_2O that was dissolved in the melt from which the NAMs crystallized (Extended Data Fig. 3). Water compatibility in the phases we analysed varies in the order melt > feldspar > clinopyroxene > orthopyroxene > olivine[33,83–85]. Given the low water concentrations in our samples, we consider phases in which H_2O is most compatible to provide the most reliable estimate of maximum parental-melt H_2O contents. Applying this argument, we can place upper bounds of 13 μg g^{-1} H_2O in NWA 11558 and NWA 8409 parental melts, 38 μg g^{-1} H_2O in NWA 6962 (based on our analyses of four melt inclusions from this sample), about 200 μg g^{-1} H_2O in NWA 2788 and NWA 6704 and about 700 μg g^{-1} H_2O in NWA 8777 and NWA 10132. We note that most published partition coefficients are experimentally determined under terrestrial conditions[33] that may not be relevant to the conditions experienced by our achondrites in terms of their bulk composition and oxygen fugacity. Wherever possible, we have chosen partition coefficients most relevant to planetary applications (for example, for water partitioning in feldspar, we applied a partition coefficient that was determined under lunar conditions[83]). We also took into account the well-known dependence of pyroxene composition on the pyroxene–melt water partition coefficient[84,85]. We also note that estimates of parental-melt H_2O contents based on mineral–melt partitioning are strict upper bounds owing to the proximity of our measured water contents to the detection limit, and the true water contents of the parental melts are probably much lower. For example, olivine in equilibrium with the melt inclusions measured in NWA 6962 (containing 10–38 μg g^{-1} H_2O) would be expected to contain approximately 0.01–0.05 μg g^{-1} H_2O; that is, the true water concentrations in the meteorite NAMs may be 1–2 orders of magnitude lower than the detection limit of our analyses. With this limitation in mind, we can estimate upper bounds on the water content of the parent bodies of our studied meteorites.

To relate the calculated water concentrations of the melts from which the meteorites crystallized to the water concentrations of their parent bodies, we must estimate the degree of partial melting of the parent body that produced the parental melts. NWA 6704 has a broadly chondritic composition for all but the most volatile elements, suggesting that its parental melt and protolith did not undergo notable segregation of metal or silicate minerals[66,69] (although note that there is evidence that paired meteorite NWA 6693 segregated sulfides[69]). We can therefore assume that NWA 6704 probably crystallized from a chondritic precursor that melted above its liquidus (that is, a melt fraction of 100%). NWA 10132 has very similar phase proportions and compositions to NWA 6704 (refs. [49,86]), so we infer that the petrogenesis of NWA 6704 and NWA 10132 were probably similar. The other orthopyroxene-rich meteorites (NWA 8777 and NWA 2788) exhibit metamorphic textures and it has been suggested that these meteorites may represent thermally metamorphosed chondritic precursors[68]. It is unclear whether or not NWA 8777 and NWA 2788 experienced any partial melting, so it is not possible at this stage to relate the water content of these meteorites to a water content of their parent bodies. Olivine-rich NWA 6962 is thought to be derived from partial melting of a CR-chondrite-like precursor[65]; however, the melt fraction required to produce NWA 6962 has not yet been constrained. Petrographic analysis of NWA 6962 shows this olivine-rich meteorite to be similar to brachinites[64]. Assuming that NWA 6962 and the brachinites had similar petrogenetic histories, it is possible that NWA 6962 formed from an approximately 30% partial melt of its precursor[34]. If so, our measurement of 10–38 μg g^{-1} H_2O in olivine-hosted melt inclusions corresponds to a parent-body water content of about 3–13 μg g^{-1} H_2O (Extended Data Fig. 4). Finally, our crustal-lithology meteorites (andesitic NWA 11558 and gabbroic NWA 8409) probably crystallized from melts produced by a relatively small degree of melting (less than about 15% (ref. [87])). If we assume that NWA 11558 feldspar crystals, in which we measured <0.62 μg g^{-1} H_2O, formed from a 15% partial melt of their parent body, we calculate that the parent body contained about 2.5 μg g^{-1} H_2O. We note that the above estimates of parent-body water content are made using a batch melting model. This approach requires fewer assumptions than more complex incremental melting models and enables ease of comparison with batch melting calculations used to estimate the bulk water content of the angrite and eucrite parent bodies[40,41]. Future work to constrain the petrogenesis of our studied meteorites may establish that incremental melting models are more appropriate than the batch melting model assumed here; however, we note that previous work has found that the aggregate melt produced during incremental melting is 'virtually identical' in terms of its highly incompatible elements to the melt produced by batch melting after the same total degree of melting[88]. Therefore, unless our meteorites happen to represent a discrete melt increment rather than an aggregate melt, the results of incremental melting models would give similar results to our batch melting calculations.

Similar arguments can be made to constrain upper bounds on the concentrations of F, S and Cl in hypothetical melts that would be in equilibrium with the NAM analyses reported in Extended Data Fig. 2, and the results of such calculations are shown in Extended Data Fig. 3 (partition coefficients used for these calculations are provided in the Supplementary Data Tables). These calculations demonstrate that the relative volatile enrichments observed in the crustal lithologies (NWA 11558 andesite and NWA 8409 gabbro; Extended Data Figs. 2 and 3) do not translate to relative enrichments of volatiles in the melts from which the meteorites crystallized compared with the more primitive meteorites in our sample suite. This is a result of the relative compatibility of volatiles in feldspar and clinopyroxene that dominate the crustal lithologies[33,41,84,89–91] compared with olivine and orthopyroxene, which dominate the more primitive lithologies[33,85,90]. A surprising result of these calculations is the high F concentration (about 4,750 μg g^{-1}) in NWA 11558 melt, despite the otherwise volatile-depleted nature of the calculated melt composition for this sample (H_2O < 13 μg g^{-1}, S < 1 μg g^{-1}, Cl < 43 μg g^{-1}) and the volatile-depleted nature of NWA 8709, which is thought to originate from the same parent body. The origin of the high F concentration in NWA 11558 plagioclase is unclear but is consistent with enrichment in the melt during partial melting of the parent body and subsequent fractional crystallization, followed by degassing at low pressure; for example, degassing experiments of lunar basaltic melt at 1 atm under reducing conditions indicate that the vapour phase evolves towards F enrichment[92].

How and when were volatiles lost from achondrite meteorites and their parent bodies?. Our results demonstrate that ungrouped achondrite meteorites are extremely volatile-depleted and therefore that melted materials did not deliver substantial quantities of volatiles to Earth. However, the timing and mechanism of volatile loss from the achondrites remains uncertain. We know that achondrite meteorites formed from thermal metamorphism and/or melting of chondritic precursor materials, and there are many opportunities for heating and volatile loss along this path:

(1) Some or all of the chondritic precursor materials may have accreted from a hot region of the nebula such that the precursor materials may have been volatile-depleted before accretion[11]. This may be particularly relevant for the NC achondrites that accreted in the inner Solar System. However, there is evidence that NC materials such as the ordinary chondrites accreted water ice[13], and recent work has suggested that the H contents of enstatite chondrites may account for the entire water budget of Earth[19]. We consider it unlikely that the CC parent bodies accreted dry because CC iron meteorites (thought to represent the cores of CC achondrite parent bodies) are much more oxidized than NC iron meteorites, suggesting that the CC iron meteorites formed in bodies that were initially ice-rich and reaction with this ice oxidized some of the Fe (ref. [36]). The presence of vesicles in CC achondrite NWA 6704 is also suggestive of a hydrous precursor[37].

(2) The chondritic precursor materials may have accreted early enough (less than about 1.5 Myr after calcium–aluminium-rich inclusions) to experience heating from the decay of short-lived radionuclides such as ^{26}Al. Depending on the timing of accretion and the size of the parent body, this heating may have been sufficient to cause global melting and differentiation (favoured for large, early-formed bodies)[23,26]. Alternatively, the heat produced may have only been sufficient to thermally metamorphose the interior of the parent body, leaving an external crust of unmetamorphosed material[24]. Either way, heating by ^{26}Al is expected to drive volatile loss.

(3) Heating during impact events on the parent bodies probably resulted in surficial or global magma oceans[24]. Outgassing of these magma oceans would drive volatile loss from the parent bodies[57].

The composition of the chondritic precursor material and the mechanism of volatile loss governs the speciation and proportion of volatiles that are outgassed. Thermal metamorphism of carbonaceous chondrite material is thought to generate H_2O-rich vapour[55,56], whereas thermal metamorphism of ordinary and enstatite chondrite material leads to the generation of CH_4-rich vapour[27,55]. Models of magma-ocean degassing find that dominant H-bearing species in the equilibrium vapour varies depending on the oxygen fugacity of the magma[57] and the pressure at the melt–vapour interface[58]. Reducing conditions (more reducing than the iron–wüstite buffer) favour H_2 over H_2O (ref. [57]). Similarly, low pressures (≪1 bar) favour H_2 over H_2O (ref. [58]).

In summary, volatile loss from planetesimals may occur by means of a range of mechanisms. The composition of vapour outgassed from planetesimals depends on their initial composition, temperature, pressure and oxygen fugacity. It is not possible with the data available to explain the exact mechanism and conditions of volatile loss that resulted in the volatile depletion of our achondrite meteorites; however, existing models and experiments suggest that the dominant H-bearing species outgassed during thermal metamorphism was probably CH_4 or H_2O and the dominant H-bearing species generated by magma-ocean degassing was probably H_2O or H_2. In the following section, we calculate the parent-body size that would be required to gravitationally retain a putative atmosphere dominated by CH_4, H_2O or H_2.

Calculation of minimum planetesimal size required to retain H-bearing species in a putative atmosphere during thermal metamorphism and/or magma-ocean outgassing. Figure 3 presents a calculation of the critical radius required for a growing planetesimal to retain vapour molecules produced during thermal metamorphism and/or magma-ocean outgassing[93]. The critical radius is calculated by setting the root-mean-squared velocity of a molecule of an ideal gas equal to its escape velocity (that is, the velocity required for a molecule of gas to escape the gravitational attraction of the planetesimal).

The root-mean-squared velocity of a molecule of an ideal gas ($\upsilon_{\rm gas}$, in m s^{-1}) is given by:

$$\upsilon_{\rm gas} = \sqrt{\frac{3k_{\rm B}T}{M_{\rm gas}}}$$

in which $k_{\rm B}$ is the Boltzmann constant, T is temperature in kelvin and $M_{\rm gas}$ is the mass of the molecule in kg. The escape velocity ($\upsilon_{\rm esc}$, in m s^{-1}) of a molecule of gas evaporated from the surface of a planetesimal with radius $r_{\rm planet}$ (in m) and mass $M_{\rm planet}$ (in kg) is given by:

$$\upsilon_{\rm esc} = \sqrt{\frac{2GM_{\rm planet}}{r_{\rm planet}}}$$

in which G is the gravitational constant. Note that $M_{\rm planet} = \rho_{\rm planet} \times \frac{4}{3}\pi r_{\rm planet}^3$, in which $\rho_{\rm planet}$ is the density of the planetesimal in kg m^{-3}. By setting $\upsilon_{\rm gas} = \upsilon_{\rm esc}$ and solving for $r_{\rm planet}$, the critical radius required for vapour-molecule retention at the surface of a growing planetesimal ($r_{\rm critical}$, in m) can be expressed as:

$$r_{\rm critical} = \frac{3}{4}\sqrt{\frac{2k_{\rm B}T}{G\pi M_{\rm gas}\rho_{\rm planet}}}$$

Data availability

All data are available in the main text, Methods or Supplementary Data Tables. Supplementary Data Tables are available at https://doi.org/10.5281/zenodo.7308443. Source data are provided with this paper.

59. Gattacceca, J., Mccubbin, F. M., Bouvier, A. & Grossman, J. The Meteoritical Bulletin, No. 107. *Meteorit. Planet. Sci.* **55**, 460–462 (2020).
60. Huyskens, M. H., Sanborn, M. E., Yin, Q. Z. & Agee, C. B. in *Proc. 49th Lunar and Planetary Science Conference*, LPI contribution no. 2083, id. 2311 (2018).
61. Srinivasan, P. et al. Silica-rich volcanism in the early solar system dated at 4.565 Ga. *Nat. Commun.* **9**, 3036 (2018).
62. Goodrich, C. A. et al. Petrogenesis and provenance of ungrouped achondrite Northwest Africa 7325 from petrology, trace elements, oxygen, chromium and titanium isotopes, and mid-IR spectroscopy. *Geochim. Cosmochim. Acta* **203**, 381–403 (2017).

63. Dunlap, D. R., Ku, Y. J., Garvie, L. A. J. & Wadhwa, M. in *46th Lunar and Planetary Science Conference*, LPI contribution no. 1832, p. 2570 (2015).
64. Ruzicka, A., Grossman, J., Bouvier, A., Herd, C. D. K. & Agee, C. B. The Meteoritical Bulletin, No. 101. *Meteorit. Planet. Sci.* **50**, 1661–1661 (2015).
65. Abe, D., Mikouchi, T. & Irving, A. J. in *Proc. 52nd Lunar and Planetary Science Conference*, LPI contribution no. 2548, id. 1813 (2021).
66. Hibiya, Y. et al. The origin of the unique achondrite Northwest Africa 6704: constraints from petrology, chemistry and Re–Os, O and Ti isotope systematics. *Geochim. Cosmochim. Acta* **245**, 597–627 (2019).
67. Sanborn, M. E., Yin, Q.-Z., Irving, A. J. & Bunch, T. E. in *Proc. 46th Lunar and Planetary Science Conference*, LPI contribution no. 1832, p. 2259 (2015).
68. Bunch, T. E., Irving, A. J., Rumble, D. & Korotev, R. L. Evidence for a carbonaceous chondrite parent body with near-TFL oxygen isotopes from unique metachondrite Northwest Africa 2788. American Geophysical Union, Fall Meeting 2006, abstracts id. P51E-1246 (2006).
69. Warren, P. H. et al. Northwest Africa 6693: a new type of FeO-rich, low-Δ^{17}O, poikilitic cumulate achondrite. *Geochim. Cosmochim. Acta* **107**, 135–154 (2013).
70. Yin, Q.-Z., Wimpenny, J. & Amelin, Y. Al-Mg systematics in the ungrouped achondrites NWA 6704. *Meteorit. Planet. Sci. Suppl.* **76**, 5160 (2013).
71. Barnes, J. J. et al. Accurate and precise measurements of the D/H ratio and hydroxyl content in lunar apatites using NanoSIMS. *Chem. Geol.* **337–338**, 48–55 (2013).
72. Hauri, E. SIMS analysis of volatiles in silicate glasses, 2: isotopes and abundances in Hawaiian melt inclusions. *Chem. Geol.* **183**, 115–141 (2002).
73. Koga, K., Hauri, E., Hirschmann, M. & Bell, D. Hydrogen concentration analyses using SIMS and FTIR: comparison and calibration for nominally anhydrous minerals. *Geochem. Geophys. Geosyst.* **4**, 1019 (2003).
74. Mosenfelder, J. L. et al. Analysis of hydrogen in olivine by SIMS: evaluation of standards and protocol. *Am. Mineral.* **96**, 1725–1741 (2011).
75. Kumamoto, K. M., Warren, J. M. & Hauri, E. H. New SIMS reference materials for measuring water in upper mantle minerals. *Am. Mineral.* **102**, 537–547 (2017).
76. Long, G. L. & Winefordner, J. D. Limit of detection. A closer look at the IUPAC definition. *Anal. Chem.* **55**, 712A–724A (1983).
77. Hirschmann, M. M., Withers, A. C., Ardia, P. & Foley, N. T. Solubility of molecular hydrogen in silicate melts and consequences for volatile evolution of terrestrial planets. *Earth Planet. Sci. Lett.* **345–348**, 38–48 (2012).
78. Bell, D. R., Rossman, G. R., Maldener, J., Endisch, D. & Rauch, F. Hydroxide in olivine: a quantitative determination of the absolute amount and calibration of the IR spectrum. *J. Geophys. Res. Solid Earth* **108**, 2105 (2003).
79. Withers, A. C., Bureau, H., Raepsaet, C. & Hirschmann, M. M. Calibration of infrared spectroscopy by elastic recoil detection analysis of H in synthetic olivine. *Chem. Geol.* **334**, 92–98 (2012).
80. Mosenfelder, J. L. & Rossman, G. R. Analysis of hydrogen and fluorine in pyroxenes: I. Orthopyroxene. *Am. Mineral.* **98**, 1026–1041 (2013).
81. Warren, J. M. & Hauri, E. H. Pyroxenes as tracers of mantle water variations. *J. Geophys. Res. Solid Earth* **119**, 1851–1881 (2014).
82. King, P. L. et al. Analytical techniques for volatiles: a case study using intermediate (andesitic) glasses. *Am. Mineral.* **87**, 1077–1089 (2002).
83. Lin, Y., Hui, H., Li, Y., Xu, Y. & Van Westrenen, W. A lunar hygrometer based on plagioclase-melt partitioning of water. *Geochem. Perspect. Lett.* **10**, 14–19 (2019).
84. O'Leary, J. A., Gaetani, G. A. & Hauri, E. H. The effect of tetrahedral Al^{3+} on the partitioning of water between clinopyroxene and silicate melt. *Earth Planet. Sci. Lett.* **297**, 111–120 (2010).
85. Dobson, P. F., Skogby, H. & Rossman, G. R. Water in boninite glass and coexisting orthopyroxene: concentration and partitioning. *Contrib. Mineral. Petrol.* **118**, 414–419 (1995).
86. Bouvier, A., Gattacceca, J., Agee, C., Grossman, J. & Metzler, K. The Meteoritical Bulletin, No. 104. *Meteorit. Planet. Sci.* **52**, 2284–2284 (2017).
87. Collinet, M. & Grove, T. L. Widespread production of silica- and alkali-rich melts at the onset of planetesimal melting. *Geochim. Cosmochim. Acta* **277**, 334–357 (2020).
88. Collinet, M. & Grove, T. L. Incremental melting in the ureilite parent body: initial composition, melting temperatures, and melt compositions. *Meteorit. Planet. Sci.* **55**, 832–856 (2020).
89. Caseres, J. R., Mosenfelder, J. L. & Hirschmann, M. M. in *Proc. 48th Lunar and Planetary Science Conference*, LPI contribution no. 1964, id. 2303 (2017).
90. Callegaro, S. et al. The quintet completed: the partitioning of sulfur between nominally volatile-free minerals and silicate melts. *Am. Mineral* **105**, 697–707 (2020).
91. Dalou, C., Koga, K. T., Shimizu, N., Boulon, J. & Devidal, J.-L. Experimental determination of F and Cl partitioning between lherzolite and basaltic melt. *Contrib. Mineral. Petrol.* **163**, 591–609 (2012).
92. Ustunisik, G., Nekvasil, H., Lindsley, D. H. & McCubbin, F. M. Degassing pathways of Cl-, F-, H-, and S-bearing magmas near the lunar surface: implications for the composition and Cl isotopic values of lunar apatite. *Am. Mineral.* **100**, 1717–1727 (2015).
93. Young, E. D. et al. Near-equilibrium isotope fractionation during planetesimal evaporation. *Icarus* **323**, 1–15 (2019).

Acknowledgements We are grateful to E. Bullock and P. Piccoli for their assistance with SEM and EPMA analyses. We are also indebted to G. Rossman, who kindly provided a piece of synthetic forsterite for use as an analytical blank. We thank P. Warren and an anonymous reviewer for their helpful comments and we are grateful to J. VanDecar for editorial handling. Many of the ideas in this contribution were developed in close collaboration with E. Hauri, whose analytical prowess and generosity are greatly missed. Funding: NASA grant 80NSSC20K0336 (S.G.N., M.E.N., C.M.O'D.A.); NASA FINESST award 80NSSC22K0043 (L.D.P.); DTM Postdoctoral Fellowship (M.E.N.).

Author contributions Conceptualization: S.G.N., M.E.N., C.M.O'D.A. Methodology: M.E.N., J.W., L.R.N., A.R.S., K.S. Investigation: M.E.N., L.D.P., J.W. Funding acquisition: S.G.N., M.E.N., C.M.O'D.A. Writing, original draft: M.E.N., S.G.N. Writing, reviewing and editing: M.E.N., S.G.N., C.M.O'D.A., L.D.P., J.W., L.R.N., A.R.S., K.S., A.J.I.

Competing interests The authors declare no competing interests.

Additional information

Supplementary information The online version contains supplementary material available at https://doi.org/10.1038/s41586-023-05721-5.

Correspondence and requests for materials should be addressed to M. E. Newcombe.

Peer review information *Nature* thanks Paul Warren and the other, anonymous, reviewer(s) for their contribution to the peer review of this work. Peer reviewer reports are available.

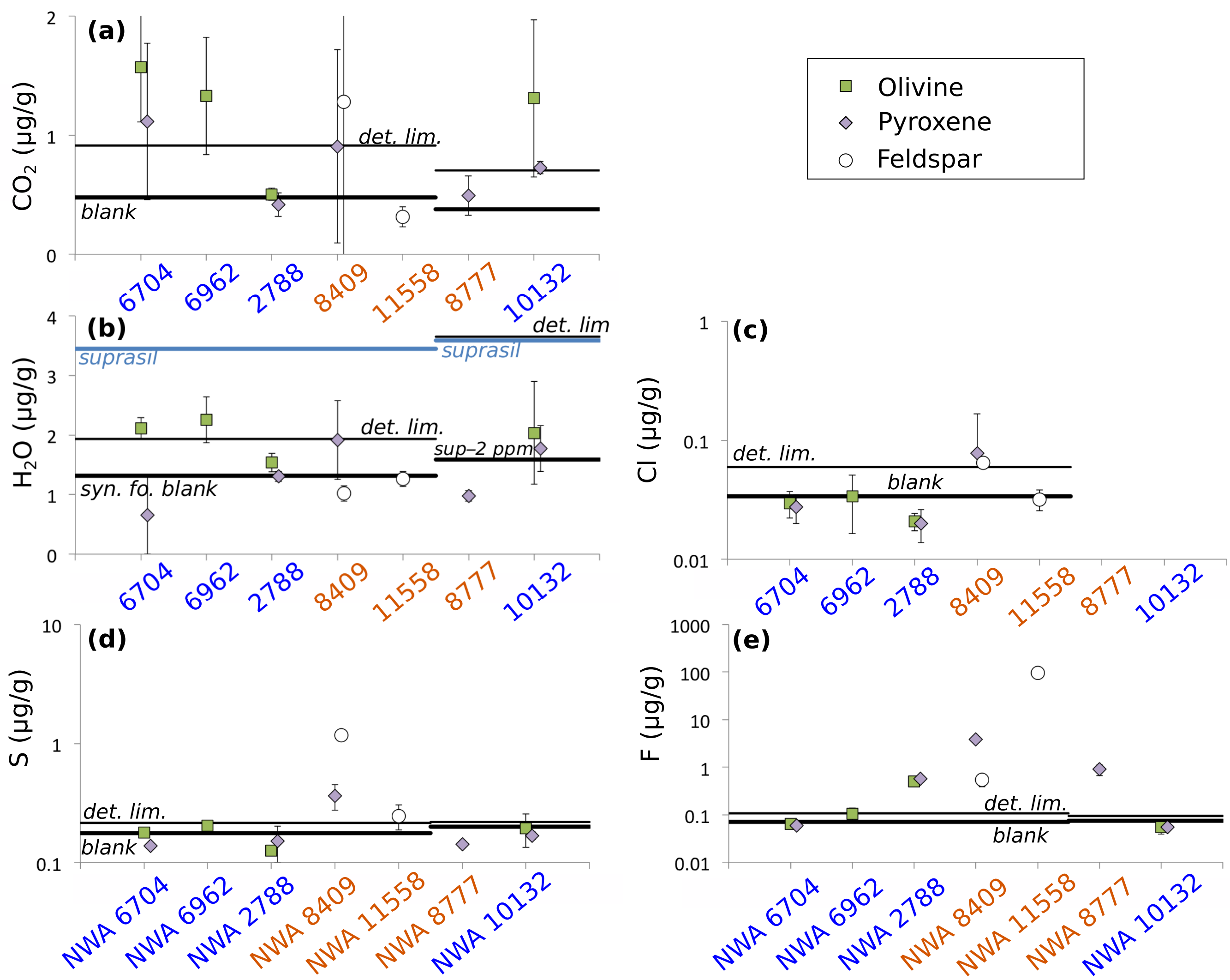

Extended Data Fig. 1 | Summary of highly volatile element analyses in CC and NC meteorite NAMs (olivine, pyroxene and feldspar). None of the analyses in this plot are blank-corrected. Error bars represent one standard deviation of replicate analyses (see Supplementary Data Tables). Data were collected during two analytical sessions: NWA 6704, NWA 6962, NWA 2788, NWA 8409 and NWA 11558 were analysed during May 2019 and NWA 8777 and NWA 10132 were analysed during March 2019. Meteorites with CC affinity are labelled in blue and meteorites with NC affinity are labelled in orange. **a**, CO_2 concentrations are primarily used to assess the impact of surface contamination; analyses were screened for outliers in $^{12}C/^{30}Si$ before their inclusion in this plot. The analytical blank and detection limit (labelled det. lim.) were assessed using Suprasil glass during the March session and synthetic forsterite during the May session. **b**, H_2O concentration data. The analytical blank and detection limit were assessed using Suprasil glass during the March session (assumed to contain 2 µg g^{-1} H_2O) and synthetic forsterite (assumed to contain 0 µg g^{-1} H_2O) during the May session. **c**, Cl concentration data. The analytical blank and detection limit were assessed using replicate analyses of synthetic forsterite. **d**, S concentration data. The analytical blank and detection limit were assessed using replicate analyses of Suprasil. **e**, F concentration data. The analytical blank and detection limit were assessed using replicate analyses of Suprasil.

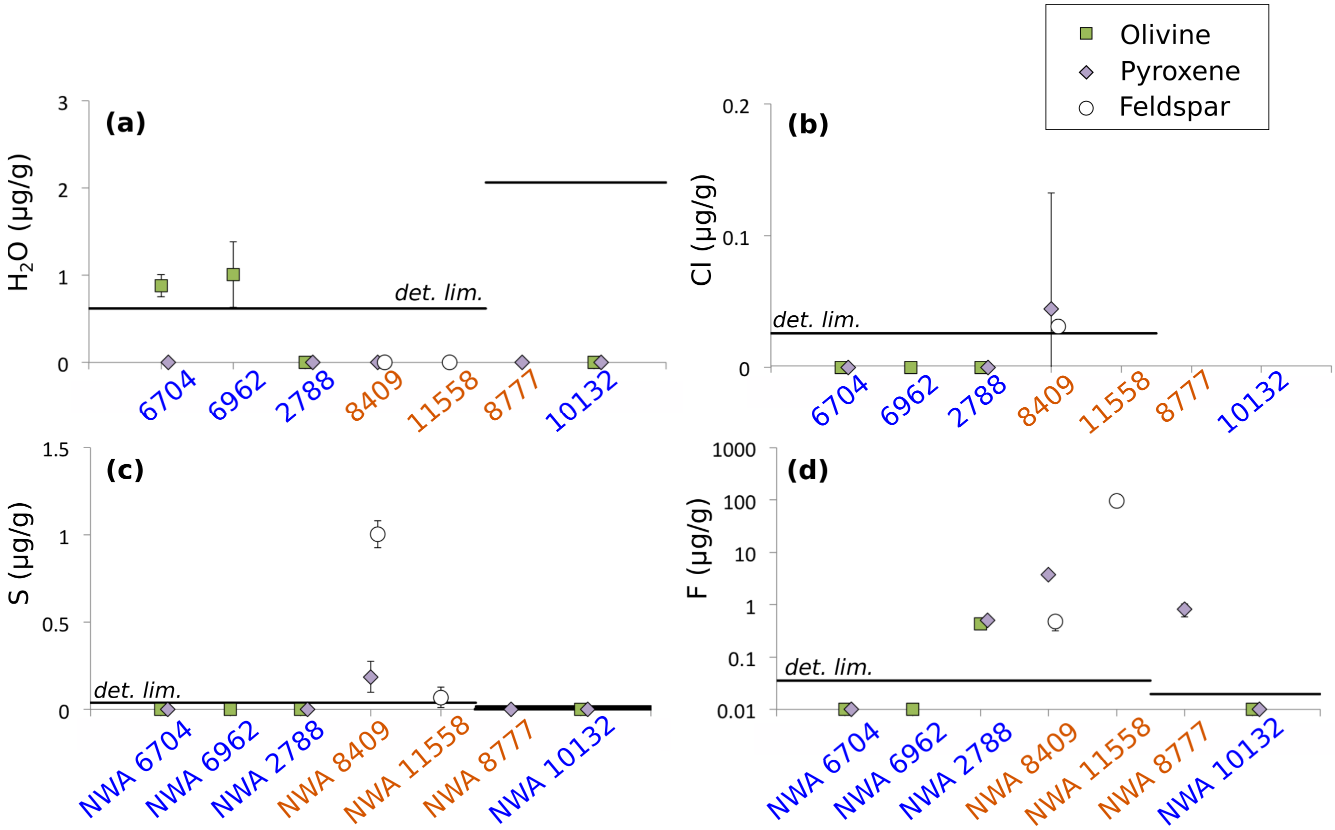

Extended Data Fig. 2 | Blank-corrected highly volatile element analyses in CC and NC meteorite NAMs (olivine, pyroxene and feldspar). Details of the analyses are provided in the caption to Extended Data Fig. 1. Error bars represent one standard deviation of replicate analyses (see Supplementary Data Tables). **a**, Blank-corrected H_2O data. Analyses below the detection limit (labelled det. lim.) are plotted at 0 µg g^{-1}. **b**, Blank-corrected Cl data. Analyses below the detection limit are plotted at 0 µg g^{-1}. Only NWA 8409 contains detectable Cl. Cl was not analysed in NWA 8777 or NWA 10132. **c**, Blank-corrected S data. Analyses below the detection limit are plotted at 0 µg g^{-1}. **d**, Blank-corrected F data. Analyses below the detection limit are plotted at 0.01 µg g^{-1}.

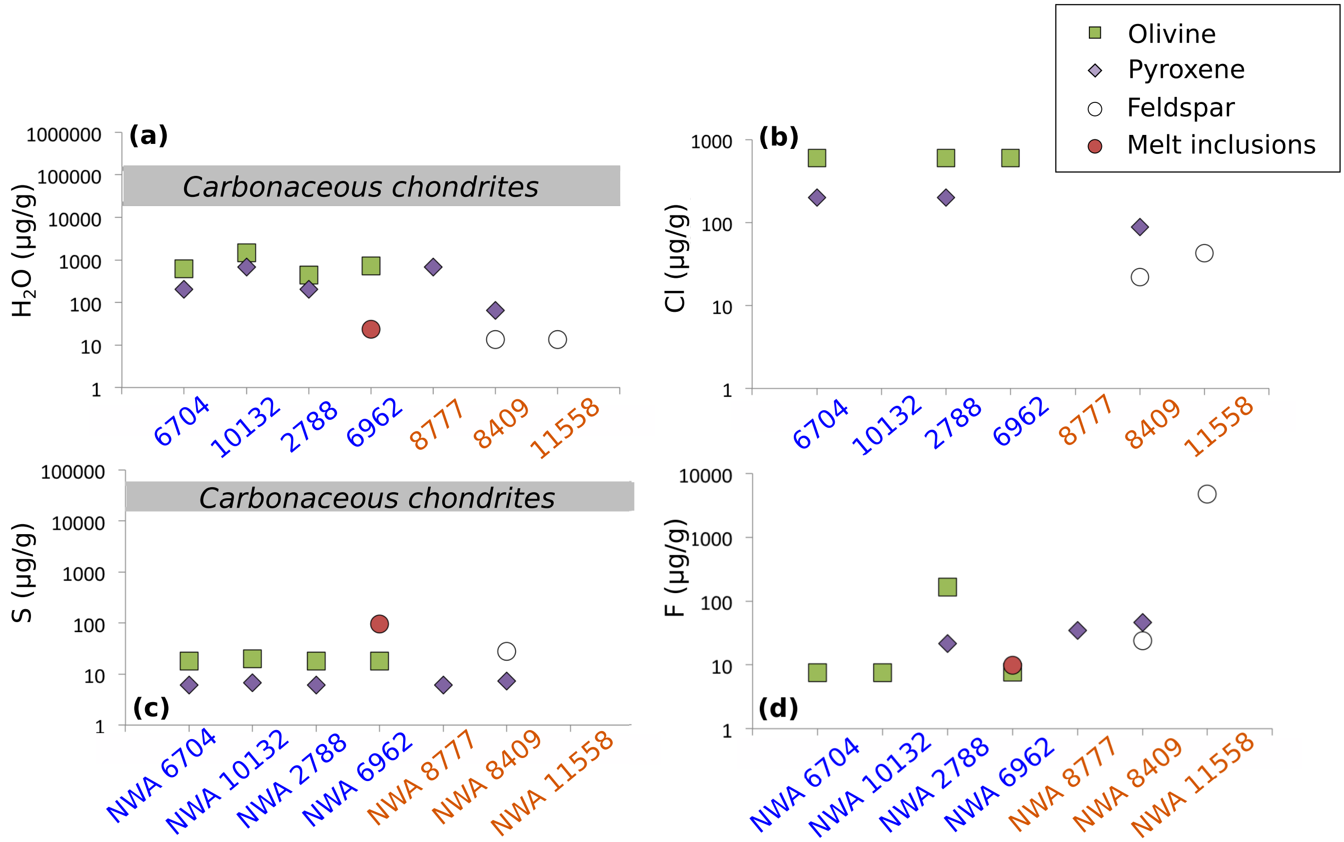

Extended Data Fig. 3 | Calculated upper bounds on the concentrations of H_2O (a), Cl (b), S (c) and F (d) in hypothetical silicate melts that would be in equilibrium with the NAMs in the CC (labelled in blue) and NC (labelled in orange) ungrouped achondrites. Concentrations are calculated using mineral–melt partition coefficients[30–32]. Ranges of H_2O and S measured in bulk carbonaceous chondrites are shown in grey[56]: the ungrouped achondrites contain at least one order of magnitude less H_2O than the driest (CV) carbonaceous chondrites and more than two orders of magnitude lower S than the most S-depleted (CK) carbonaceous chondrites.

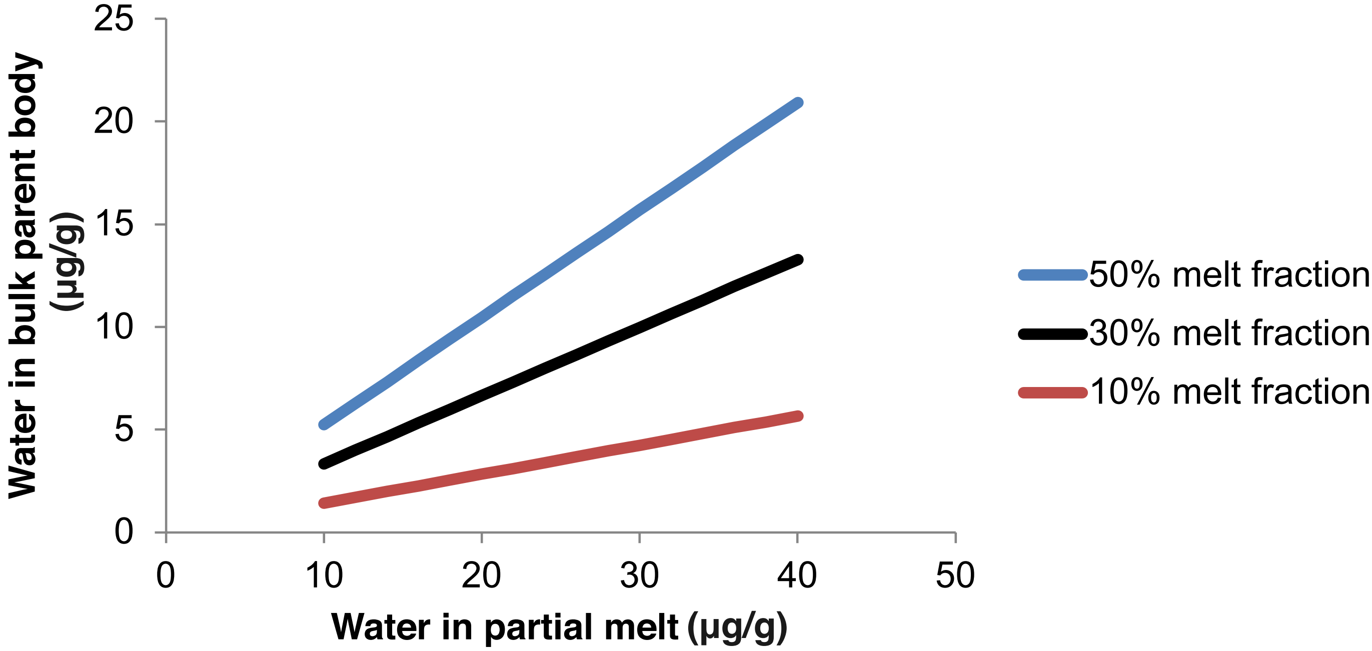

Extended Data Fig. 4 | Calculated H_2O in the NWA 6962 parent body assuming that the precursor material underwent 10%, 30% and 50% batch melting and assuming that the water concentrations measured in olivine-hosted melt inclusions from this sample (containing 10–38 µg g^{-1} H_2O) are representative of primitive mantle melts. The petrogenetic history of NWA 6962 is poorly constrained but its olivine-rich mineralogy is petrographically similar to the NC brachinite meteorites that are thought to have been generated by crystallization of an approximately 30% partial melt of chondrite-like precursor materials[35]. Assuming a melt fraction of 30%, we estimate that the NWA 6962 parent body contained about 3–13 µg g^{-1} H_2O.

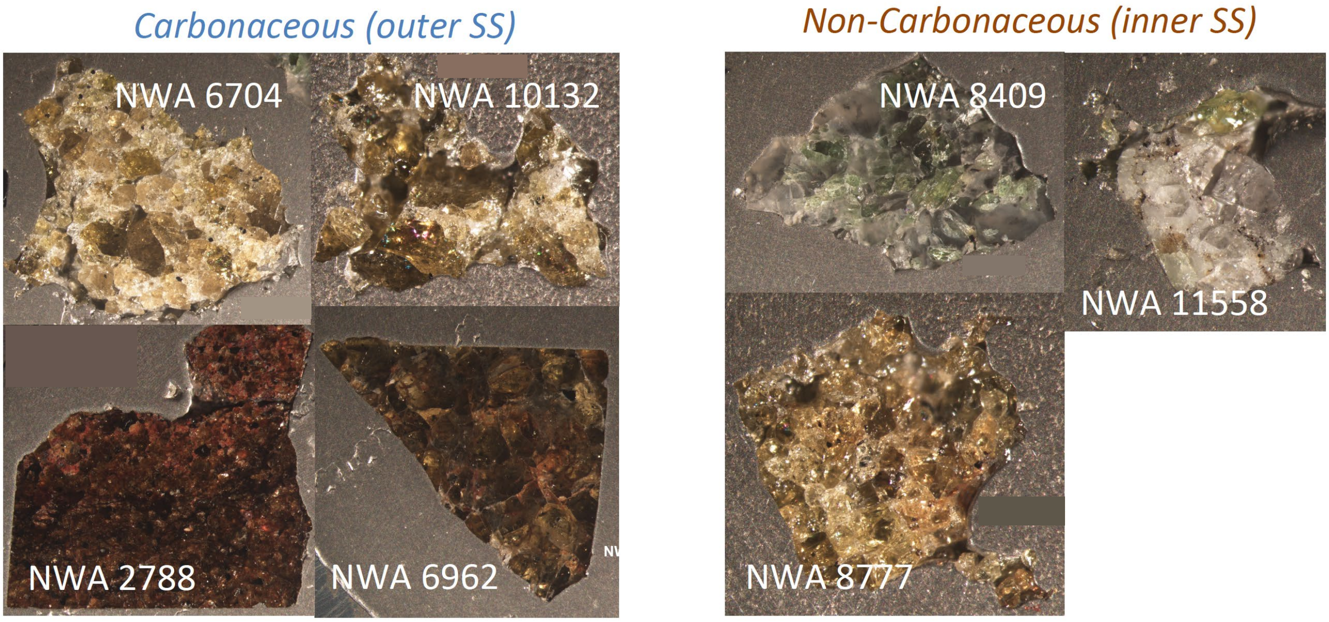

Extended Data Fig. 5 | Photomicrographs of the meteorite chips analysed during this study. All chips are a few millimetres across; scale bars for individual chips are provided in Extended Data Figs. 6–12. Chips are pressed into indium.

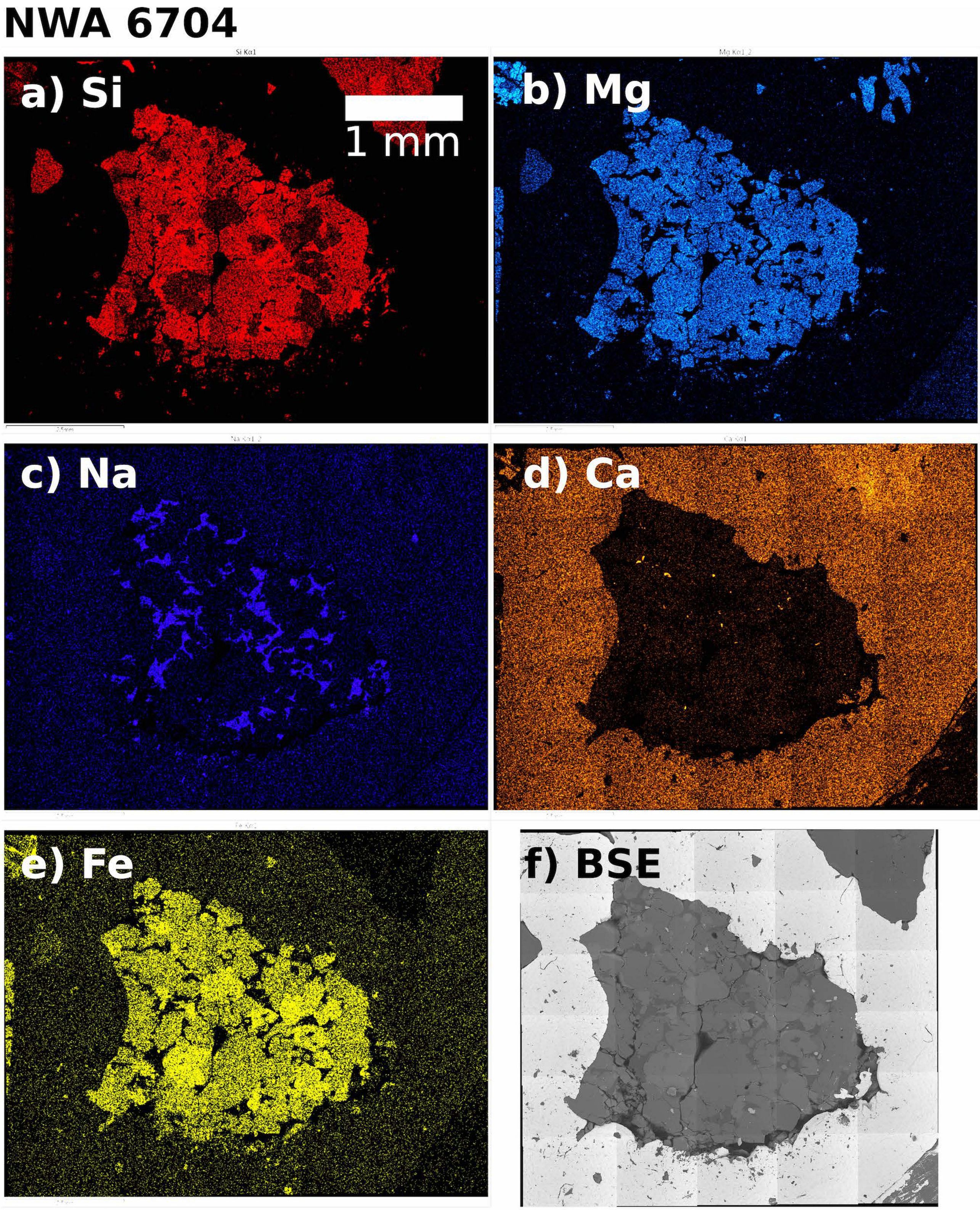

Extended Data Fig. 6 | Elemental concentration maps measured by EDS and BSE image of NWA 6704. **a**–**e**, Elemental concentration maps. **f**, BSE image.

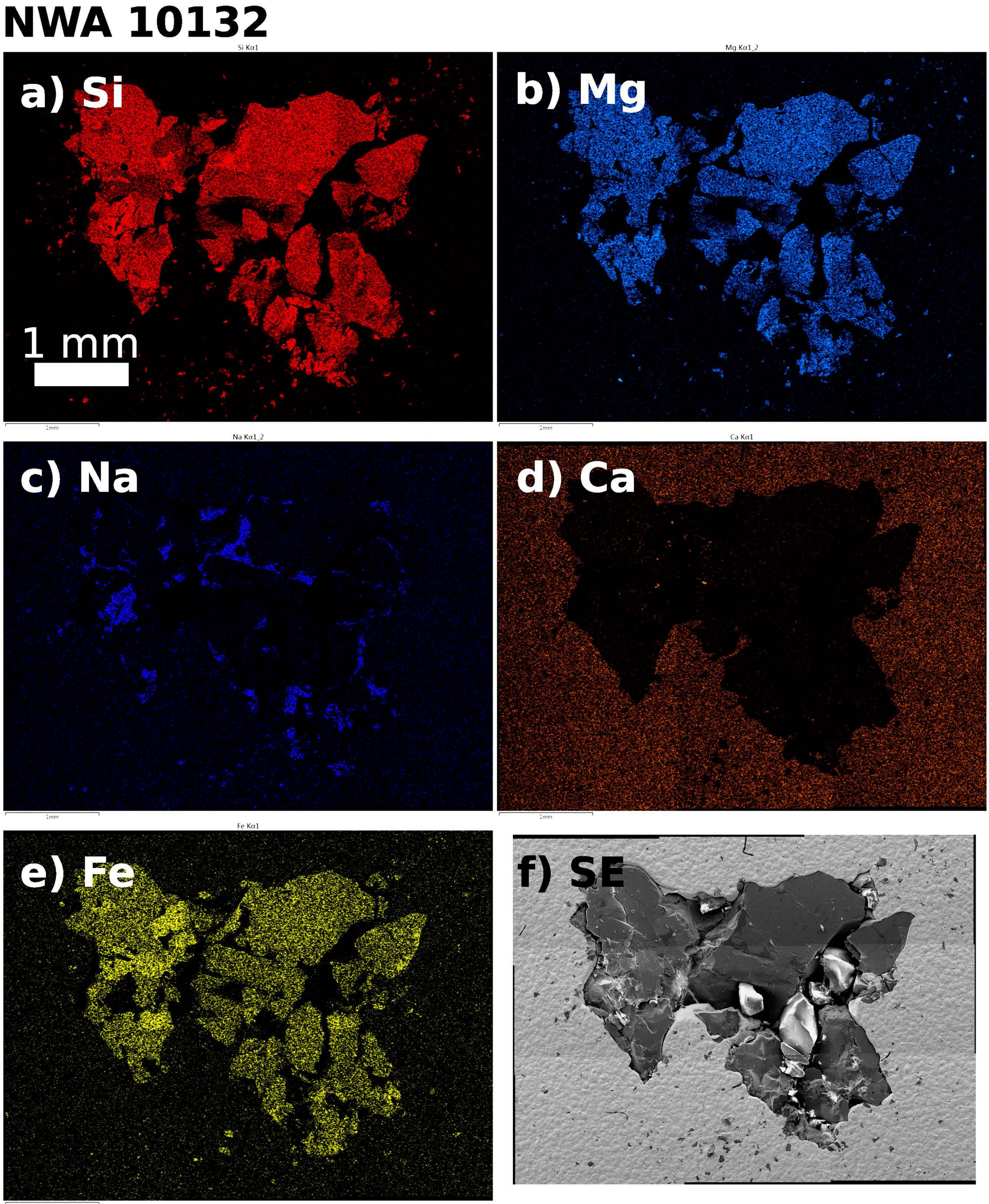

Extended Data Fig. 7 | Elemental concentration maps measured by EDS and secondary electron image of NWA 10132. a–e, Elemental concentration maps. **f**, Secondary electron image.

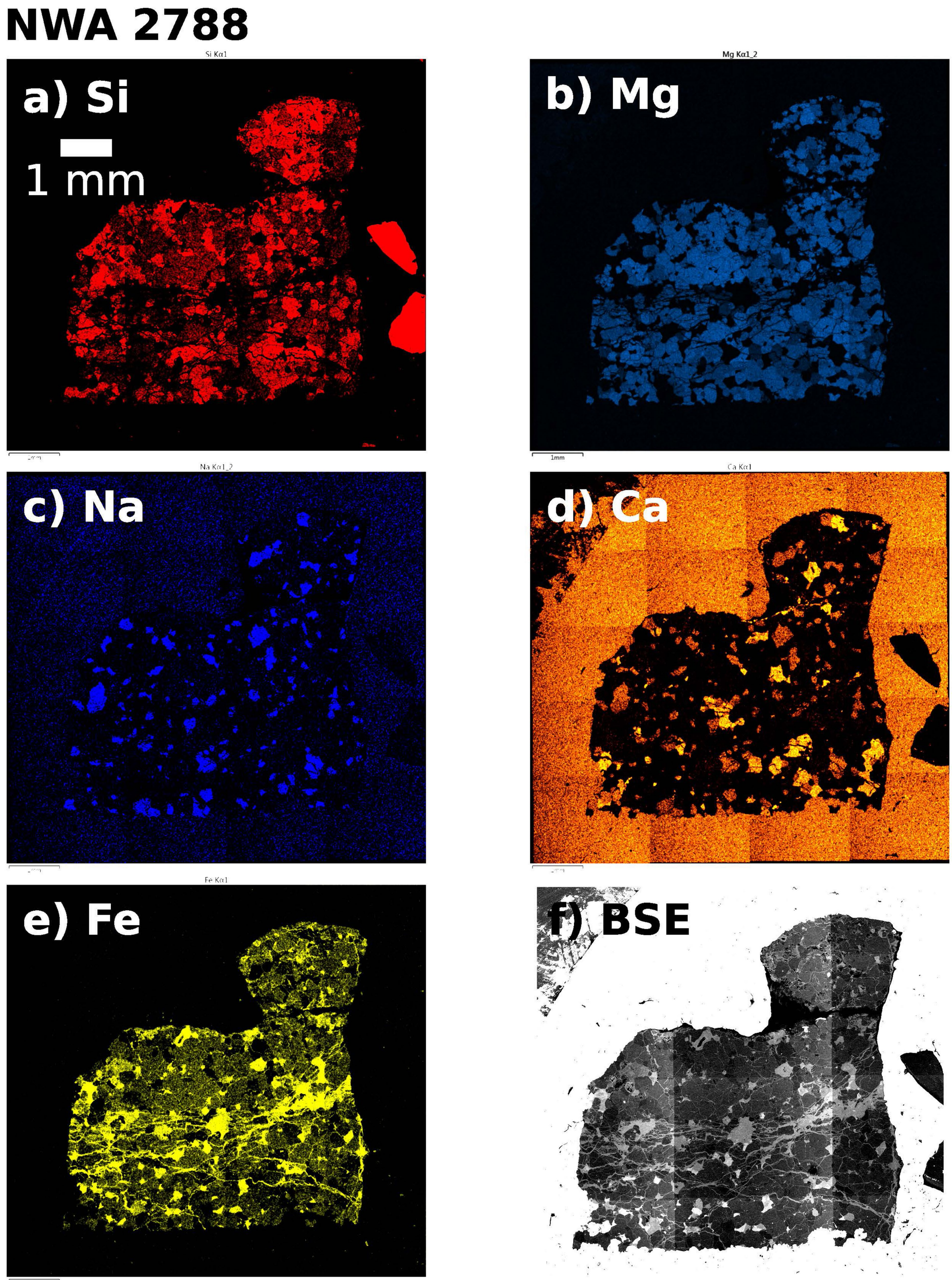

Extended Data Fig. 8 | Elemental concentration maps measured by EDS and BSE image of NWA 2788. **a**–**e**, Elemental concentration maps. **f**, BSE image.

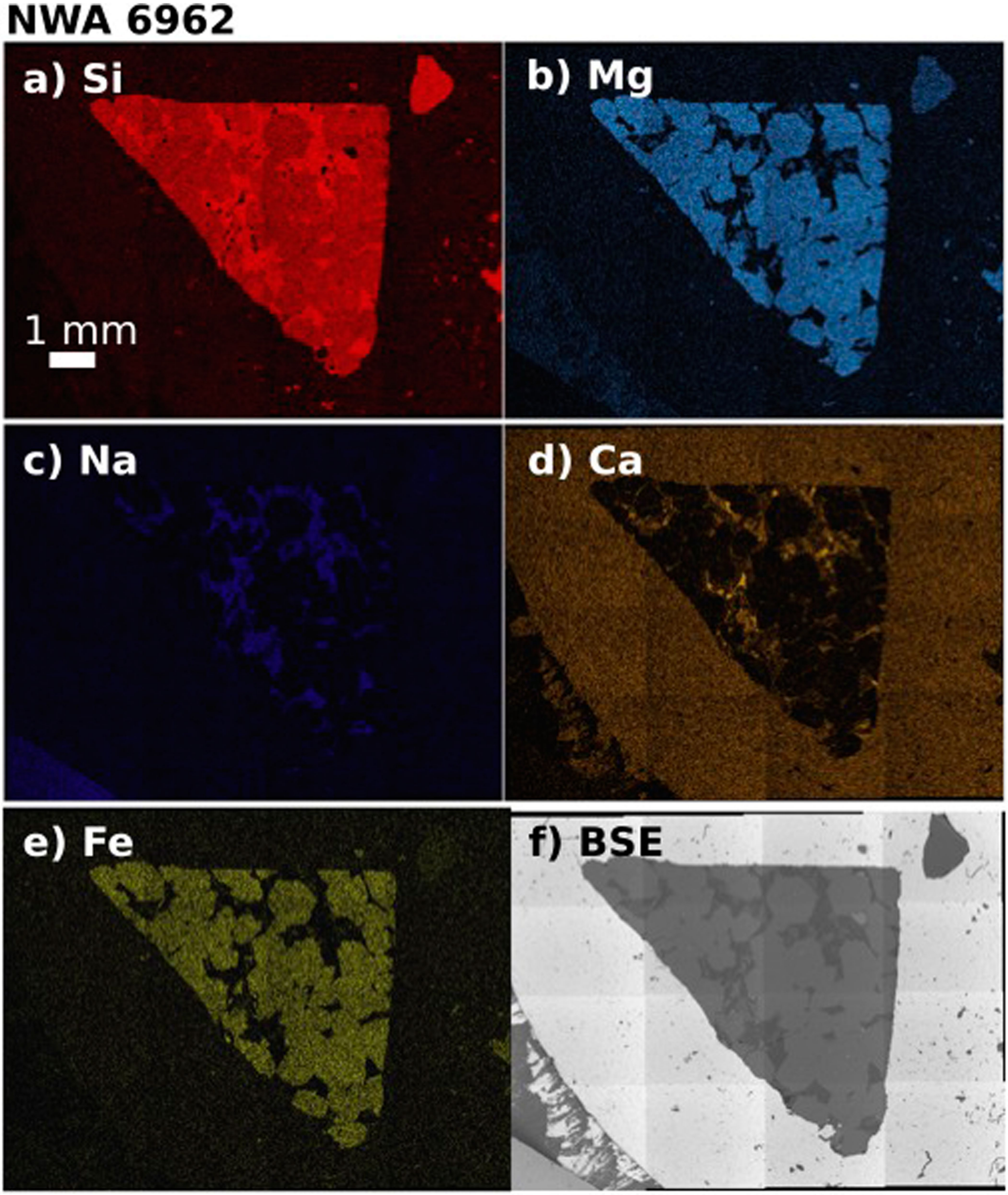

Extended Data Fig. 9 | Elemental concentration maps measured by EDS and BSE image of NWA 6962. **a**–**e**, Elemental concentration maps. **f**, BSE image.

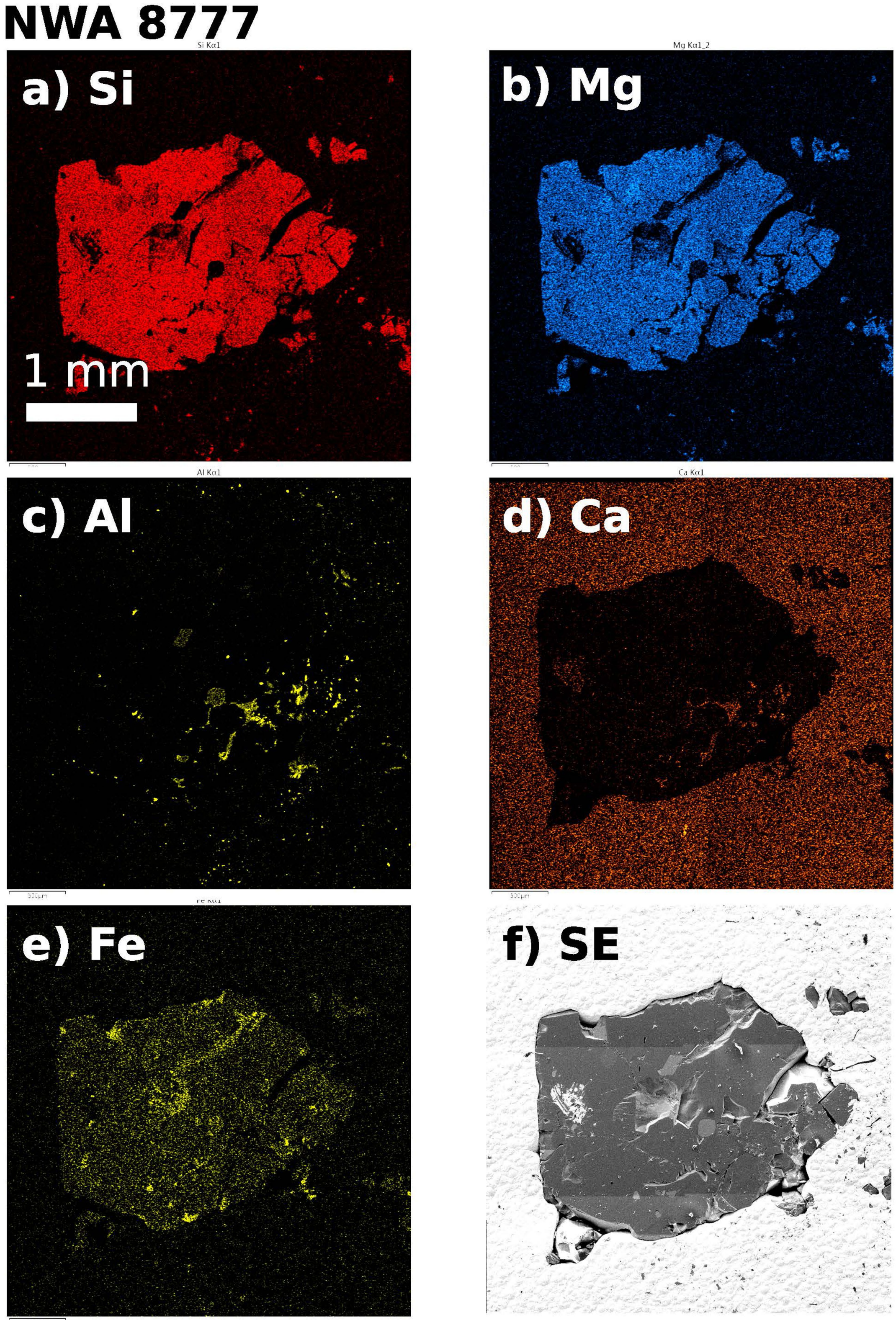

Extended Data Fig. 10 | Elemental concentration maps measured by EDS and secondary electron image of NWA 8777. a–e, Elemental concentration maps. **f**, Secondary electron image.

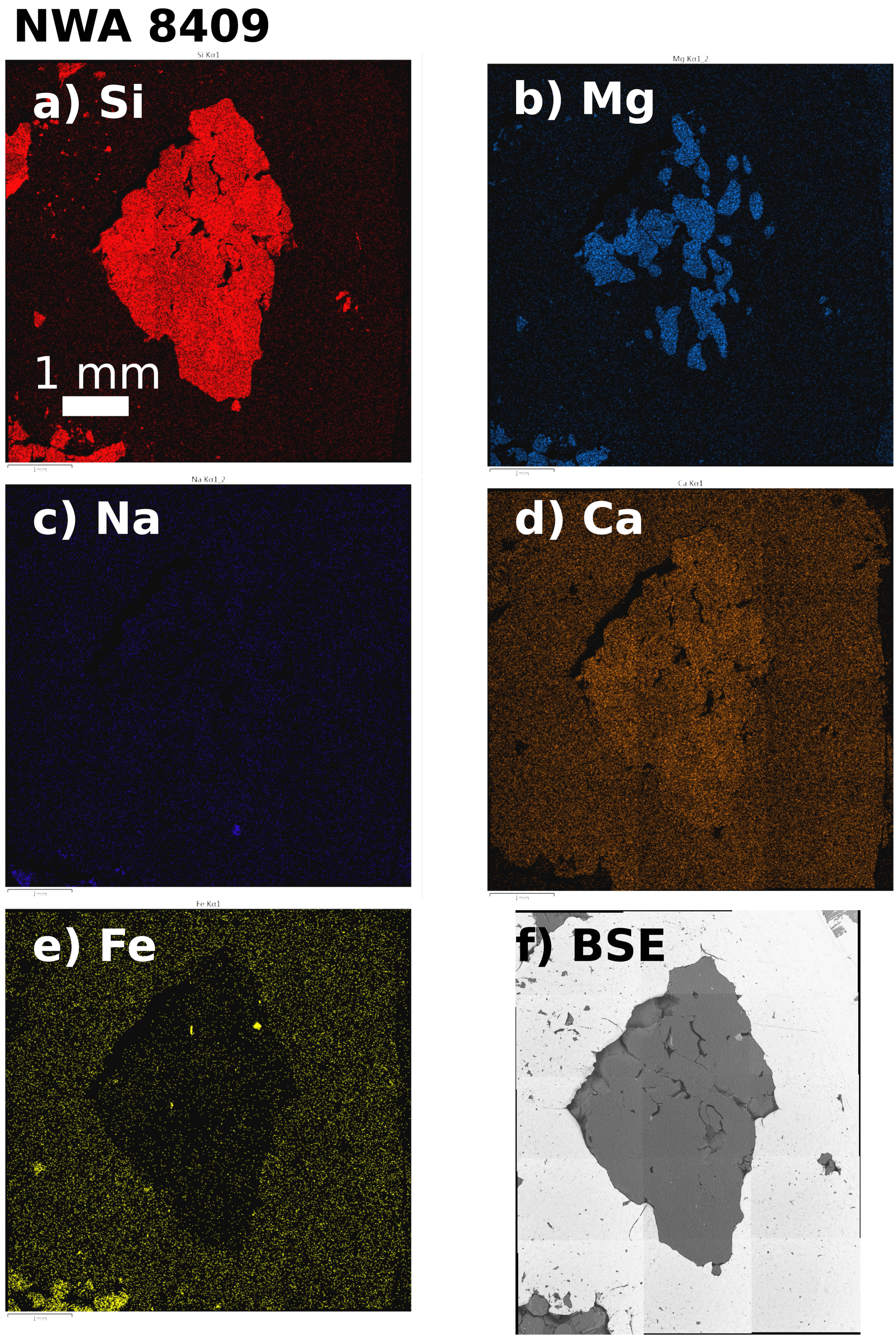

Extended Data Fig. 11 | Elemental concentration maps measured by EDS and BSE image of NWA 8409. a–e, Elemental concentration maps. **f**, BSE image.

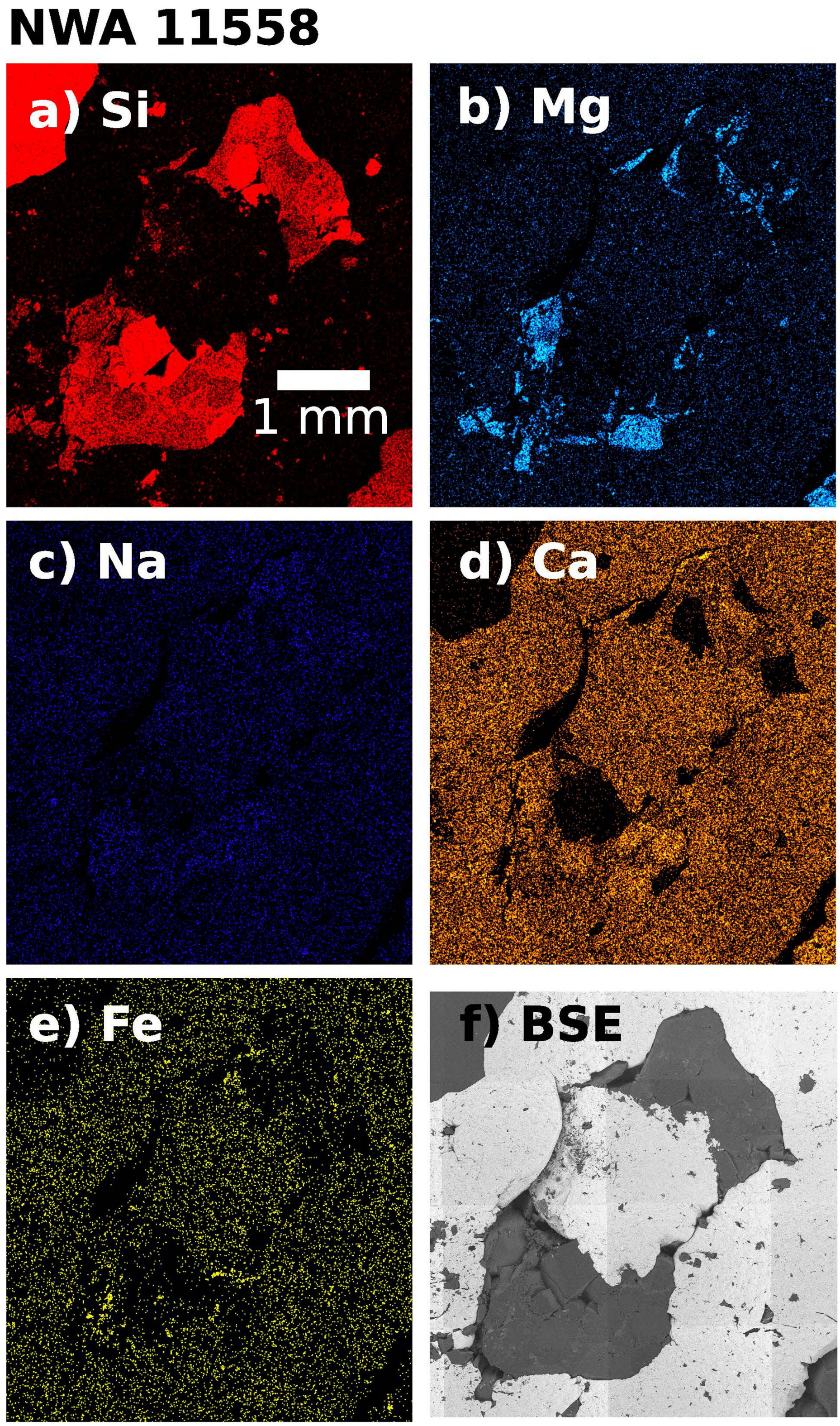

Extended Data Fig. 12 | Elemental concentration maps measured by EDS and BSE image of NWA 11558. a–e, Elemental concentration maps. **f**, BSE image.